

Research Articles: Systems/Circuits

Astrocytes sustain circadian oscillation and bidirectionally determine circadian period, but do not regulate circadian phase in the suprachiasmatic nucleus

<https://doi.org/10.1523/JNEUROSCI.2337-21.2022>

Cite as: J. Neurosci 2022; 10.1523/JNEUROSCI.2337-21.2022

Received: 26 November 2021

Revised: 20 March 2022

Accepted: 3 May 2022

This Early Release article has been peer-reviewed and accepted, but has not been through the composition and copyediting processes. The final version may differ slightly in style or formatting and will contain links to any extended data.

Alerts: Sign up at www.jneurosci.org/alerts to receive customized email alerts when the fully formatted version of this article is published.

Copyright © 2022 Patton et al.

This is an open-access article distributed under the terms of the Creative Commons Attribution 4.0 International license, which permits unrestricted use, distribution and reproduction in any medium provided that the original work is properly attributed.

1

2

3

4

5

Astrocytes sustain circadian oscillation and bidirectionally determine circadian period, but do not

6

regulate circadian phase in the suprachiasmatic nucleus.

7

8

19 words, 155 chrs.

9

10

Short title: Astrocytic and neuronal control of SCN timekeeping.

11

12

13

Andrew P. Patton¹, Nicola J. Smyllie¹, Johanna E. Chesham¹ and Michael H. Hastings^{1*}

14

15

¹Address: MRC Laboratory of Molecular Biology, Francis Crick Avenue, Cambridge, CB2 0QH, UK

16

* Corresponding Author. email: mha@mrc-lmb.cam.ac.uk

17

18

The authors declare no financial interests or conflicts of interest.

19

20 **Abstract**

21

22 The suprachiasmatic nucleus (SCN) is the master circadian clock of mammals, generating and
23 transmitting an internal representation of environmental time that is produced by the cell-autonomous
24 transcriptional/post-translational feedback loops (TTFL) of the 10,000 neurons and 3,500 glial cells.
25 Recently, we showed that TTFL function in SCN astrocytes alone is sufficient to drive circadian
26 timekeeping and behaviour, raising questions about the respective contributions of astrocytes and
27 neurons within the SCN circuit. We compared their relative roles in circadian timekeeping in mouse
28 SCN explants, of either sex. Treatment with the glial-specific toxin fluorocitrate revealed a
29 requirement for metabolically competent astrocytes for circuit-level timekeeping. Recombinase-
30 mediated genetically complemented Cryptochrome (Cry) proteins in Cry1- and/or Cry2-deficient SCN,
31 were used to compare the influence of the TTFLs of neurons or astrocytes in the initiation of *de novo*
32 oscillation or in pacemaking. While neurons and astrocytes both initiated *de novo* oscillation and
33 lengthened period equally, their kinetics were different: astrocytes taking twice as long. Furthermore,
34 astrocytes could shorten period, but not as potently as neurons. Chemogenetic manipulation of Gi-
35 and Gq-coupled signalling pathways in neurons acutely advanced or delayed ensemble phase,
36 respectively. In contrast, comparable manipulations in astrocytes were without effect. Thus,
37 astrocytes can initiate SCN rhythms and bi-directionally control SCN period, albeit with lower potency
38 than neurons. Nevertheless, their activation does not influence SCN phase. The emergent SCN
39 properties of high amplitude oscillation, initiation of rhythmicity, pacemaking and phase are
40 differentially regulated: astrocytes and neurons sustain the ongoing oscillation, but its phase is
41 determined by neurons.

42

43 250/250 words

44

45

46 **Significance Statement**

47 The hypothalamic suprachiasmatic nucleus (SCN) encodes and disseminates time-of-day information
48 to allow mammals to adapt their physiology to daily environmental cycles. Recent investigations have
49 revealed a role for astrocytes, in addition to neurons, in regulation of this rhythm. Using
50 pharmacology, genetic complementation and chemogenetics, we compared the abilities of neurons
51 and astrocytes in determining the emergent SCN properties of high amplitude oscillation, initiation of
52 rhythmicity, pacemaking and determination of phase. These findings parameterise the circadian
53 properties of the astrocyte population in the SCN, and reveal the types of circadian information
54 astrocytes and neurons can contribute within their heterogeneous cellular network.

55

56 100/120 words

57 **Introduction**

58 Mammalian behavioural and physiological circadian rhythms are orchestrated by the hypothalamic
59 suprachiasmatic nucleus (SCN), which is synchronised to environmental time via the
60 retinohypothalamic tract (RHT) (Reppert and Weaver, 2002) (Patton and Hastings, 2018). This retinal
61 innervation is not, however, required for the SCN to create and broadcast a representation of
62 environmental time: SCN timekeeping in isolation *ex vivo* is robust and can persist with precision near
63 indefinitely, sustaining rhythms ranging between <16 to >42 hours across a range of genetic and
64 pharmacological manipulations (Patton et al., 2016). This robustness arises from strong, presumably
65 reciprocal, network interactions between the approximately 10,000 neurons and 3,500 glia, including
66 astrocytes (Hastings et al., 2018).

67 At its core, timekeeping in the majority of cells in the body is directed by the activity of a
68 transcriptional-translational feedback loop (TTFL) whereby Period (Per) and Cryptochrome (Cry)
69 proteins act on the transcription factors CLOCK and BMAL1 to repress their own transcription (Partch
70 et al., 2014). This generates a rhythmic alternation of activation and repression, over the course of
71 approximately 24 hours, of the *Per* and *Cry* genes and their transcriptional targets. It is this TTFL-
72 based oscillation, welded into the strong network architecture of the SCN that produces robust
73 timekeeping at the circuit level. This is characterised by emergent properties of high amplitude
74 precise oscillation, tightly defined ensemble period and phase, and spatially complex cellular
75 synchrony (Hastings et al., 2018; Patton et al., 2020).

76 Until recently, the γ -amino butyric acid (GABA)-ergic and neuropeptidergic neurons were thought to
77 be the major SCN timekeeping component, becoming electrically and metabolically active in the
78 middle of circadian day and quiescent during circadian night (Colwell, 2011; Brancaccio et al., 2017).
79 Consistent with this view, recent intersectional genetic approaches (reviewed in (Patton et al., 2020))
80 have revealed that SCN neurons together, as a whole, are sufficient for maintaining and initiating
81 circadian rhythms in the SCN *ex vivo* and *in vivo* (Lee et al., 2015) (Maywood et al., 2018; Brancaccio
82 et al., 2019) as well as setting the relative phase (Jones et al., 2015) and determining the dynamics of
83 the ongoing oscillation (Lee et al., 2015) (Brancaccio et al., 2013).

84 Alongside these approaches in neurons, recent studies have also revealed astrocytes as active
85 participants in the SCN network. Astrocytes display robust rhythms in TTFL function (Tso et al., 2017;

86 Brancaccio et al., 2019) and cytosolic calcium ($[Ca^{2+}]_i$) (Brancaccio et al., 2017), sitting in antiphase to
87 neuronal rhythms (Brancaccio et al., 2017; Brancaccio et al., 2019). Additionally, the astrocytic TTFL
88 clock is sufficient to determine SCN and behavioural period (Brancaccio et al., 2017; Tso et al., 2017)
89 and even initiate rhythmicity in an otherwise “clockless” SCN, driving neuronal $[Ca^{2+}]_i$ rhythms and
90 behavioural rhythms (Brancaccio et al., 2019). In contrast to this initiation, disruption of the astrocytic
91 TTFL lengthens behavioural and *ex vivo* SCN period (Barca-Mayo et al., 2017; Tso et al., 2017).
92 Furthermore, manipulation of a putative astrocyte-neuron adenosine/cannabinoid signalling axis can
93 induce phase-shifts during the circadian day (Hablitz et al., 2020). Astrocytes can therefore impose
94 their circadian state upon SCN neurons and the whole animal, potentially via three mechanisms that
95 modulate GABA-ergic signalling: active release of glutamate by astrocytes (Brancaccio et al., 2017);
96 active GABA uptake contributing to a vasoactive intestinal polypeptide (VIP)/GABA balance (Barca-
97 Mayo et al., 2017); or astrocytic adenosine release (Hablitz et al., 2020).

98 These findings raise the question of the relative potency of astrocytes, as compared to neurons, in
99 determining the circadian properties of the SCN circuit. Using pharmacology, calcium imaging,
100 intersectional genetics and chemogenetic manipulation we therefore compared the abilities and
101 strengths of astrocytes and neurons to determine the emergent, ensemble timekeeping properties of
102 the SCN: high amplitude oscillation, rhythm initiation, period and phase. We show that whereas
103 astrocytes are powerful regulators of the on-going, steady-state SCN oscillation, their activation does
104 not contribute to resetting the ensemble oscillation to a new phase: entrainment is mediated by
105 neuronal activity.

106

107 646/650 words

108

109

110 **Materials and Methods**

111

112 **Animals**

113 All experiments were performed in accordance with the UK Animals (Scientific Procedures) Act of
114 1986, with local ethical approval (MRC LMB AWERB). Per2::Luciferase mice were kindly supplied by
115 J.S. Takahashi, University of Texas Southwestern Medical Centre, USA (Yoo et al., 2004). Cry1-null,
116 Cry2-null and Cry1,2-null (Cry-null) animals were derived from founders kindly supplied by G. van der
117 Horst, Erasmus University Medical Centre, Rotterdam, NL (van der Horst et al., 1999). Cry1-null,
118 Cry2-null and Cry-null mice were crossed to the Per2::Luciferase line in-house. All lines were
119 maintained on a C57BL/6J background.

120

121 **AAVs and molecular biology**

122 For Cry-complementation experiments, Cre-conditional Cry1::EGFP (*pCry1-DIO.Cry1::EGFP*) was
123 packaged by Penn Vector Core as AAV1 serotype from a plasmid backbone produced in-house
124 (Brancaccio et al., 2019). The Cre-conditional Cry2::EGFP (*pCry2-DIO.CRY2::EGFP*) AAV was
125 generated by first modifying AAV.*pCry1(min)-mCry2::EGFP* (Edwards et al., 2016) through
126 replacement of the minimal *pCry1* promoter with a minimal *pCry2* promoter (Smyllie et al., 2022). The
127 coding sequence was inverted and double-inverted-orientation LoxP sites added to create a Cre-
128 inducible version before being packaged as AAV1 serotype (Vector Builder).
129 pZac2.1.gfaABC1D.cyto-GCaMP6f (*GFAP-cytoGCaMP6f*) was a gift from Baljit Khakh (UCLA)
130 (Addgene viral prep #52925-AAV5; RRID:Addgene_52925) (Haustein et al., 2014). The
131 chemogenetic constructs hM3D(Gq) and hM4D(Gi) under the control of either the *hSyn* or *GFAP*
132 promoters were a gift from Bryan Roth (UNC) and supplied via Addgene as follows:
133 pAAV.GFAP.hM3D(Gq)::mCherry.WPRE.bGHpA (*GFAP-hM3Dq::mCherry*) (Addgene viral prep
134 #50478-AAV5; RRID:Addgene_50478); pAAV.GFAP.hM4d(Gi)::mCherry.WPRE.bGHpA (*GFAP-*
135 *hM4Di::mCherry*) (Addgene viral prep #50479-AAV5; RRID:Addgene_50479),
136 pAAV.hSyn.hM3D(Gq)::mCherry.WPRE.bGHpA (*Syn-hM3Dq::mCherry*) (Addgene viral prep #50474-
137 AAV8; RRID:Addgene_50474) and pAAV.hSyn.hM4d(Gi)::mCherry.WPRE.bGHpA (*Syn-*

138 hM4Di::mCherry) (Addgene viral prep #50475-AAV8, RRID:Addgene_50475). Cre-recombinase
139 AAVs (*hSyn*-mCherry::Cre and *GFAP*-mCherry::Cre) were AAV8 serotype (UNC Vector Core).
140 pAAV.EF1a.DIO.EYFP (*EF1a*-DIO.EYFP) was a gift from Karl Deisseroth (Stanford) (Addgene viral
141 prep #27056-AAV1; RRID:Addgene_27056).

142

143 **Organotypic slice preparation and AAV transduction**

144 Mice (P10-12) of either sex were sacrificed according to local and UK Home Office rules, the brain
145 removed, and the SCN dissected before being sliced coronally and cultured as an explant via the
146 interface method for one week (Hastings et al., 2005). The culture medium was then changed, and
147 slices were transduced with 1 μ l AAV (>1 \times 10¹² GC/ml in PBS) applied directly to the top of the slice.
148 Slices were then left a further week before medium was changed. Where slices received more than
149 one transduction, this was performed serially with 24 hours between medium change and AAV
150 application. Successful transduction was confirmed by imaging of the encoded fluorescent reporter.

151

152 **Real-time bioluminescent and fluorescent imaging**

153 Bioluminescence was monitored in real-time in customised light-tight incubators equipped with
154 photon-multiplier tubes (PMTs) (Hamamatsu H9319-11 photon counting head), before data were
155 binned at 6-minute intervals for export. SCN slices were maintained in HEPES-buffered medium
156 containing DMEM, supplemented with Glutamax, penicillin/streptomycin, FCS, B27 and luciferin in
157 dishes sealed with glass coverslips as previously described (Patton et al., 2016).

158 For combined circadian fluorescent/ bioluminescent recordings, SCN slices were maintained in
159 sealed, glass-bottomed imaging dishes (Mattek) with the same medium as in PMT recordings and
160 imaged on an LV200 system (Olympus) (Brancaccio et al., 2013). Dependent on the experimental
161 configuration, bioluminescence was acquired for between 9.5 and 29.5 minutes, while simultaneous
162 fluorescence acquisition was set at 100ms (EYFP, mCherry) or 250ms (GCaMP6f). Acquisition
163 intervals for combined circadian imaging were 30 minutes.

164 For calcium imaging of SCN slices to test acute DREADD activation, vehicle (PBS) or 100nM
165 clozapine-N-oxide (CNO) (in PBS) were added as a 1 μ l drop directly to the surface of the slice on the

166 heated stage of an LV200 system. Due to the rapid kinetics of the response in *GFAP-*
167 *hM4Di::mCherry* and *GFAP-cytoCaMP6f* co-expressing slices (Figure 4), recordings were made
168 using the GFP channel at an acquisition rate of 5Hz with the exposure interval set to 100ms. Due to
169 the comparatively slower kinetics of the response in *GFAP-hM3Dq::mCherry* and *GFAP-*
170 *cytoCaMP6f* co-expressing slices (Figure 4), recordings were made using the GFP channel at an
171 acquisition rate of 0.5Hz with the exposure interval set to 100ms. In both experimental configurations,
172 slices were recorded for a baseline period of 1 minute before either vehicle or CNO were added to the
173 preparation and recording continued for another 5 minutes. Before and after the experiment, mCherry
174 and brightfield images were taken with exposure times of 100ms and 10ms respectively.

175

176 **Analysis of bioluminescent and fluorescent imaging**

177 All PMT data were analysed by BioDARE2 (<https://www.biodare2.ed.ac.uk>) (Moore et al., 2014;
178 Zielinski et al., 2014), using the FFT-NLLS method (Maywood et al., 2018) before additional analyses
179 were applied. In the case of rhythmic SCN genotypes, a peak-to-peak method was applied where all
180 the peaks in a recording were identified and the mean time-difference between consecutive peaks
181 taken as the period for that cycle. Where the point of initiation of rhythmicity was determined based
182 on instantaneous period, the waveclock package (Price et al., 2008) for R (R Core Team,
183 <https://www.R-project.org/>) was utilised and the period output was used to determine the timepoint at
184 which period crossed the 25 to 29h threshold (i.e., 2 hours either side of the expected initiated period
185 identified by BioDARE). This was once the timepoint was outside the cone of influence (defined as
186 $\sqrt{2} \times \text{period}$) where the reported data may be affected by “edge effects” at the beginnings and ends of
187 the time series. Rhythmicity and arrhythmicity were measured by calculating the autocorrelation of
188 recordings that were detrended by fitting a second order polynomial function at a lag of 24h (in the
189 case of wild-type comparisons) or 28h (in the case of *Cry1*-competent rhythms). Autocorrelation was
190 calculated in R using the `acf` command in the base R stats package.

191 Automated ROI analysis of real-time circadian bioluminescence imaging was performed as described
192 previously (Patton et al., 2016) using the SARFIA package (Dorostkar et al., 2010) in Igor Pro 8
193 (Wavemetrics). Recordings were represented as a false-coloured raster plot. All raster plots were
194 coloured using the viridis colour scale. Using these data, synchrony was also determined by manual

195 calculation of Rayleigh vectors in Microsoft Excel from circadian parameters determined in BioDARE2
196 (Patton et al., 2016).

197 Circadian calcium imaging data were analysed as described (Patton et al., 2020). Briefly,
198 fluorescence images were aligned manually and background subtracted in FIJI (Schindelin et al.,
199 2012) before full z-stacks were taken to obtain aggregate fluorescence signals. In the case of
200 circadian imaging, these signals were detrended and, in the fluorocitrate experiments, fluorescence
201 changes were expressed as relative amplitude by dividing the detrended data by the average of the
202 raw signal for that experimental interval. Because of the continual rise in the fluorescence baseline as
203 a function of continuing AAV-mediated expression of the reporter, this was deemed the most
204 appropriate means of normalising the data to allow comparison between different temporal windows
205 across the entire recording.

206 For analysis of calcium imaging of acutely manipulated DREADD-expressing Cry-null SCN slices,
207 aggregate signals were taken as described above following alignment and background subtraction,
208 but these recordings did not require detrending. Aggregate recordings were normalised using a (F_t/F_0)
209 F_0/F_0 method where F_0 was designated as the average of the baseline for 1 minute before treatment.
210 The peak change in this measurement was calculated by taking the average of the first 30 seconds
211 immediately following treatment. Finally, network dynamics across the SCN were examined by
212 creating raster plots using automated SARFIA ROI analysis routines as described above, but using
213 the DREADD-mCherry signal to direct ROIs to DREADD-expressing cells.

214

215 **Pharmacological treatments**

216 For fluorocitrate experiments, drug or vehicle were prepared fresh in parallel immediately before
217 treatment (Paulsen et al., 1987). Briefly, a stock solution of fluorocitrate was prepared by dissolving
218 8mg fluorocitrate barium salt in 1ml 0.1M HCl before 2-3 drops of 0.1M Na_2SO_4 were added to the
219 solution to precipitate the barium. Finally, 2ml Na_2HPO_4 was added and the solution was centrifuged
220 at 1000g for 5 minutes. The supernatant containing fluorocitrate was adjusted to pH7.4 and then
221 pipetted off and added directly to the medium at a final concentration of 50 μM . For the preparation of
222 vehicle, fluorocitrate barium salt was omitted, and an equal volume of vehicle was added to the

223 medium. Treatments were left *in situ* for up to 5 days before they were washed out by transferring the
224 slice between pre-warmed recording medium three times at 5 minutes intervals.

225 For chemogenetic experiments, DREADD-expressing slices were recorded in PMTs for at least 4
226 cycles to generate a baseline from which the phase of treatment was extrapolated. At the correct
227 phase for treatment, slices affixed to membranes were transferred to pre-warmed recording medium
228 containing either 100nM clozapine-N-oxide (CNO) or 0.01% H₂O (Vehicle). Slices were then left in
229 this medium for 1 hour before the treatment was washed out by transferring the slice between pre-
230 warmed recording medium three times at 5 minutes intervals. Finally, the slices were returned to their
231 original recording medium and recorded for at least 3 further cycles. Each slice was subjected to at
232 least two treatments at the same phase (CNO and Vehicle), the order of which was randomised in the
233 *GFAP-Gq*-, *GFAP-Gi*- and *Syn-Gi*-expressing slices. In the case of *Syn-Gq*, slices were treated with
234 vehicle before being treated with CNO as *Gq*-activation in SCN neurons has been shown previously
235 to perturb ongoing SCN function permanently through a presumed VIP-ergic mechanism (Brancaccio
236 et al., 2013; Hamnett et al., 2019). All phase shifts were assessed as paired measures where a slice
237 was subjected to vehicle and CNO at a particular phase. Any slice that did not receive both
238 treatments was excluded from analysis. Phase shifts were calculated as described (Patton et al.,
239 2020). Briefly, the 4 cycles pre-treatment were used to calculate the baseline period which was used
240 to normalise subsequent shifts in circadian time. Phase shifts were calculated as the difference
241 between the actual peaks and the predicted peaks extrapolated forward by the mean baseline period
242 from the peak preceding treatment and expressed as the mean of the three cycles following
243 treatment. Acute changes in cycle amplitude were calculated by taking the absolute difference in
244 bioluminescence between the final peak and final trough before treatment (baseline cycle) and the
245 first peak and first trough immediately following treatment (treatment cycle). This was then expressed
246 as the amplitude of the treatment cycle normalised to the baseline cycle.

247

248 **Experimental Design and Statistical Analyses**

249 For *Cry1* initiation and pacemaking experiments, the identity of the Cre-expressing AAVs was blinded.
250 Transductions with the Cre-expressing AAVs were randomly allocated to slices of the required
251 genotype in a balanced approach. The final identities of the promoters driving Cre-expression were

252 not revealed until after the initial pacemaking and initiation data were acquired and analysed (Figure 2
253 and Figure 3). In all other experiments, no blinding was applied, but where possible slices received
254 paired treatments (vehicle and drug) or were assigned randomly to groups when this was not
255 possible. All data were analysed in Microsoft Excel (Microsoft, US), R (v3.6.1, R Foundation for
256 Statistical Computing, Austria), Rstudio (v1.2.1335, Rstudio Inc, US), Igor Pro 8 (Wavemetrics, US),
257 and GraphPad Prism 9 (Graphpad, US). All the statistical tests used are listed in the text and figure
258 legends.

259

260

261 **Results**

262 ***Compromise of astrocytic metabolism reversibly disrupts SCN molecular oscillations***

263 In Cry-deficient SCN, astrocytic clocks are, alone, sufficient to initiate rhythmicity (Brancaccio et al.,
264 2019) and determine circadian period (Brancaccio et al., 2017). It is unclear, however, whether
265 astrocytic metabolic competence is required to maintain the circadian oscillation in an otherwise
266 functional SCN network. To test this, we treated SCN slices with the classical metabolic gliotoxin;
267 fluorocitrate. This inhibitor of aconitase (Fonnum et al., 1997) has been shown specifically to disrupt
268 carbon flux through the glial tricarboxylic acid (TCA) cycle (Swanson and Graham, 1994) and thereby
269 compromise astrocytic function. To confirm this effect of fluorocitrate on SCN astrocytes, we made
270 multiplexed recordings of SCN slices transduced with the specific astrocytic calcium reporter *GFAP*-
271 *cytoGCaMP6f*, expressed via AAV. This reporter revealed strong circadian rhythms of intracellular
272 calcium ($[Ca^{2+}]_i$) in the astrocytes, with a characteristic waveform as reported (Brancaccio et al.,
273 2017) (Figure 1A). Over the first 24 hours of treatment with 50 μ M fluorocitrate, but not vehicle, the
274 amplitude of $[Ca^{2+}]_i$ rhythms in astrocytes was acutely suppressed (Normalised amplitude: vehicle vs
275 fluorocitrate, 1.02 \pm 0.24 vs 0.50 \pm 0.15, paired two-tailed t-test, $t(3) = 4.71$, $p = 0.018$) (Figure 1B),
276 which persisted with sustained treatment. Treatment of SCN slices with fluorocitrate therefore
277 severely disrupted astrocytic metabolism directly, as reflected by disrupted $[Ca^{2+}]_i$ rhythms.

278 Having established the acute effect of fluorocitrate on astrocytic $[Ca^{2+}]_i$ rhythms within the intact SCN
279 network, we then assessed the effect of this metabolic disruption of astrocytes on the aggregate,
280 network-wide SCN TTFL rhythms. Aggregate bioluminescence rhythms arising from the entire
281 network were recorded in PMTs from *Per2::Luciferase* SCN before, during and after 5 days of
282 treatment with either vehicle or 50 μ M fluorocitrate (Figure 1C). Fluorocitrate treatment did not alter
283 the overall period (median Δ period from baseline: vehicle vs. fluorocitrate, 0.03 vs. 0.20 h, Mann-
284 Whitney test, $U = 158.5$, $p = 0.19$) (Figure 1D), or precision of the oscillation, as determined by the
285 relative amplitude error (RAE) (RAE ratio treatment/baseline: vehicle vs. fluorocitrate, 0.78 \pm 0.08 vs.
286 1.28 \pm 0.26 au, unpaired two-tailed Welch's t-test $t(24.51) = 1.85$, $p = 0.08$) (Figure 1E). It did, however,
287 significantly reduce the amplitude of the aggregate *Per2::Luciferase* rhythm by ~50%, compared to
288 vehicle-treated slices (Figure 1C and F) (Normalised amplitude: vehicle vs. fluorocitrate 0.55 \pm 0.02 vs
289 0.31 \pm 0.02 au, unpaired two-tailed Welch's t-test $t(38.72) = 9.08$, $p < 0.0001$). Notwithstanding the

290 gradual reduction in amplitude arising from luciferin depletion from the medium (2-way ANOVA time
291 effect, $F(3, 112) = 80.36$, $p < 0.0001$), the effect of fluorocitrate was immediate and was sustained (2-
292 way ANOVA treatment effect, $F(1, 39) = 127.4$, $p < 0.0001$) (Figure 1G) until its removal by medium
293 change. Consequently, there was no significant interaction between time and treatment (2-way
294 ANOVA time-by-treatment interaction, $F(3, 112) = 2.049$, $p = 0.1$). Upon medium change, the
295 normalised amplitude under treatment with vehicle reversed from $55 \pm 7\%$ to $97 \pm 2\%$ of the baseline
296 amplitude, while the reduction in normalised amplitude observed under fluorocitrate treatment was
297 reversed from $31 \pm 9\%$ to $80 \pm 6\%$ of the normalised amplitude. Furthermore, the immediate
298 suppressive effect of fluorocitrate on network-wide TTFL rhythms was phase-dependent, insofar as
299 the reduced amplitude of the first peak following treatment was greatest when SCN were treated
300 during the late circadian day and early circadian night (CT6-12 and CT12-18) (Figure 1C, 1H), phases
301 that correspond to the time of increasing astrocytic activity (Brancaccio et al., 2017). In SCN where
302 treatment missed this window of sensitivity, peak amplitude was not suppressed until the second
303 cycle. These data indicate that the robustness of circadian oscillation in the SCN is dependent on
304 astrocytic metabolism, and that compromise of astrocytic metabolism can reversibly suppress the
305 TTFL, likely by reducing the network reinforcement of circadian amplitude. We then investigated
306 whether the disruption caused by fluorocitrate manifested as changes in network-level synchrony by
307 imaging Per2::Luciferase bioluminescence via CCD camera. As with the ensemble signal from PMT
308 recordings (Figure 1C), treatment with fluorocitrate reduced the amplitude of TTFL rhythms in
309 individual oscillators across the network (Figure 1I and J) (normalised amplitude vehicle vs.
310 fluorocitrate 0.61 ± 0.02 vs. 0.31 ± 0.03 au, paired two-tailed t-test $t(6) = 9.38$, $p < 0.0001$). This
311 reduction in amplitude was associated with a significant reduction in synchrony under treatment with
312 fluorocitrate, as measured by Rayleigh vector length (2-way repeated measures ANOVA, treatment
313 effect $F(1,6) = 10.72$, $p = 0.017$), such that SCN treated with fluorocitrate were less synchronised than
314 before treatment (2-way repeated measures ANOVA, interval effect $F(1,6) = 15.75$, $p = 0.007$) and less
315 than vehicle-treated slices (2-way repeated measures ANOVA, treatment-by-interval interaction $F(1,6)$
316 $= 12.3$, $p = 0.013$) (Figure 1K). This reduction in synchrony is consistent with weaker cycle-on-cycle
317 reinforcement of cellular rhythms across the network caused by the reduced amplitude of the SCN
318 TTFL, itself an effect of compromised astrocytic metabolism. Metabolically compromised astrocytes
319 therefore lead to a weaker clock network.

320

321 ***Initiation of de novo rhythmicity in Cry-null SCN by astrocytes***

322 Having established that astrocytic metabolic competence is required for proper SCN function, even
323 when both astrocytes and neurons have functional TTFLs, we sought to test the relative contributions
324 of neurons and astrocytes to the *de novo* initiation of rhythmicity in the SCN. We expressed Cre-
325 conditional Cry1 under the control of the minimal Cry1 promoter (*pCry1-DIO.Cry1::EGFP*) delivered
326 via AAVs into Cry1,2-null (Cry-null), *Per2::Luciferase*-positive SCN explants. To express Cry1
327 specifically in these two cell types, Cre-recombinase was expressed under the control of either the
328 human synapsin promoter (*Syn*; *Syn-mCherry::Cre*) or the short GFAP promoter (*GFAP*; *GFAP-*
329 *mCherry::Cre*) to target neurons or astrocytes, respectively. Cry-deficient SCN slices were arrhythmic
330 during the baseline interval, up until cell-type-specific Cre released conditional Cry1::EGFP
331 expression (Figure 2A). Rhythmicity was initiated following the addition of Cre to either population,
332 stabilising over the next 20 days, and evidenced by an increase in the rhythmicity index
333 (autocorrelation at 28 h) (2-way ANOVA interval effect, $F(1,18) = 63.56$, $p < 0.0001$). By this measure,
334 there was no difference in quality between the rhythms generated by the two cell-types (2-way
335 ANOVA cell-type effect, $F(1,18) = 0.28$, $p = 0.60$) (Figure 2B). Furthermore, the rhythmicity initiated by
336 both populations stabilised with an identical period of ~27 h, regardless of the cell-type targeted
337 (neuron- vs. astrocyte-initiated 27.5 ± 0.7 vs. 27.9 ± 0.6 h, unpaired two-tailed t-test $t(18) = 0.5$, $p = 0.6$)
338 (Figure 2C). Having established that both populations can initiate rhythmicity, we then assessed this
339 initiation in intervals of 7 days, corresponding to the experimental periods covering baseline (BL),
340 post-Cry AAV transduction (AAV1), post-Cre AAV transduction (AAV2) and two serial medium
341 changes (MC1 and MC2) (Figure 2A). FFT-based analysis of PMT recordings assigned nominal
342 periods ranging between 10 and 40 h in the windows before Cre-AAV addition, which then converged
343 (2-way ANOVA time-effect, $F(4, 65) = 3.74$, $p = 0.009$) at ~27 h following the targeting of Cre to either
344 cell type (2-way ANOVA cell-type effect, $F(1, 18) = 0.09$, $p = 0.76$) (Figure 2D).

345 As the FFT-based analysis inevitably assigns nominal periods to the arrhythmic portion of the
346 recording, it is not possible to quantify whether there is a difference in initiation kinetics between the
347 two cell populations based solely on the FFT-reported period. We therefore examined the identified
348 rhythms, using the inverse metric of quality: RAE (Figure 2E). As with period, RAE displayed a large

349 range during the arrhythmic intervals before Cre was added. Following addition of the Cre-AAV,
350 however, rhythms became better organised in both cases and the RAE values converged (2-way
351 ANOVA time effect, $F(4, 65) = 8.19$, $p < 0.0001$) to the same level (neurons: 0.09 ± 0.01 ; astrocytes:
352 0.09 ± 0.01 , 2-way ANOVA cell-type effect, $F(1, 18) = 0.27$, $p = 0.61$). Furthermore, post-hoc multiple
353 comparisons to the baseline interval revealed that the neuronally initiated slices reached their final
354 RAE measurement sooner than did the astrocyte-initiated slices (neurons: 7-14 days post
355 transduction (dpt) (MC1); astrocytes: 14-21 dpt (MC2)) (Figure 2E). To assess the difference in the
356 kinetics of *de novo* rhythmicity more formally, we applied a wavelet-based analysis (Price et al., 2008)
357 to determine the time at which the algorithm detected rhythms with an instantaneous period within the
358 circadian range of 25 to 29 h. As determined by these criteria, rhythmicity was initiated in all slices
359 but the rate differed between the two cell types. The point at which the instantaneous period crossed
360 into the 25 to 29 h threshold showed that neurons initiated robust rhythmicity sooner than did
361 astrocytes (neurons vs. astrocytes 96.6 ± 16.5 vs. 179.5 ± 30.1 h, unpaired Welch's two-tailed t-test,
362 $t(13.96) = 2.41$, $p = 0.03$) (Figure 2F).

363

364 This difference in kinetics could arise from the cell-type targeted or from the relative efficiency of the
365 cell-specific promoters driving the Cre-recombinase. To assess this, we transduced SCN slices with
366 an AAV to Cre-conditionally express EYFP (*EF1a-DIO.EYFP*) and recorded a baseline. In the
367 absence of Cre-recombinase there was no detectable expression of EYFP (Figure 2G, H). Once
368 either *Syn*- or *GFAP*-driven Cre-expressing AAVs were added, however, EYFP fluorescence emerged
369 and revealed cell-type-specific morphologies (Figure 2G). Moreover, it increased over the following
370 five days at a comparable rate in both populations (Figure 2H). To quantify the kinetics of this rise,
371 we determined the time post-transduction for the normalised fluorescence signal to pass a threshold
372 of a 10% increase in signal. There was no significant difference in the time taken to reach this point
373 between the two cell-type-specific promoters (*Syn* vs *GFAP*: 71.75 ± 4.97 vs. 68.13 ± 1.68 h, unpaired
374 Welch's two-tailed t-test $t(3.672) = 0.69$, $p = 0.53$) (Figure 2H, I), indicating that differences in the rate
375 of initiation of rhythmicity by either neurons or astrocytes cannot be attributed to differential
376 expression of Cre-recombinase from the *Syn*- or *GFAP*- promoters, respectively. Thus, while both
377 neurons and astrocytes can initiate *de novo* rhythmicity with the same period and quality in an

378 otherwise clock-less SCN, astrocytes take much longer than do neurons to impose their cell-
379 autonomous TTFL time-keeping across the full circuit.

380

381 ***Bidirectional control of SCN period by astrocytes***

382 The network of Cry1,2-null circadian-incompetent neurons may provide a permissive context for the
383 imposition of astrocytic cell-autonomous time-keeping across the SCN. A potentially more demanding
384 test of astrocytic influence is the ability to impose their cell-autonomous properties on an otherwise
385 circadian-competent SCN. We therefore applied the same dual-transduction approach to express
386 either Cry1 or Cry2 in an attempt to lengthen or shorten the period of rhythmic short-period Cry1-null
387 or long-period Cry2-null SCN, respectively. How effectively can astrocytes act as pacemakers and
388 determine the period of an ongoing stable oscillation? In the absence of any Cre-expression, Cry1-
389 null SCN slices transduced with *pCry1-DIO.Cry1::EGFP* exhibited a short (~22 h) period (Figure 3A,
390 B). Cell-selective expression of Cre-recombinase lengthened the period of both treatment groups
391 over the following 20 days, to ultimately stabilise at ~23.5 h (2-way ANOVA interval effect, $F(1, 20)$
392 =39.09, $p<0.0001$) (Figure 3B), and with no difference between SCN in which either of the two cell-
393 types were targeted (2-way ANOVA cell-type effect, $F(1, 20) =0.03$, $p =0.86$) (Figure 3B, C). Coarse,
394 longitudinal assessment of FFT-assessed period over successive time windows confirmed that the
395 period lengthened progressively (2-way ANOVA interval effect, $F(3, 60) =33.46$, $p<0.0001$), and the
396 final period was not significantly different between the two targeted cell populations (2-way ANOVA
397 cell-type effect, $F(1, 20) =3.64$, $p =0.07$). However, despite the fact that both populations could
398 equally lengthen period, explants in which neurons were targeted reached their stable final period at
399 an earlier experimental interval than did SCN in which the period was lengthened by the astrocytes
400 (2-way ANOVA cell-type/interval interaction, $F(3, 60) =4.35$, $p =0.008$) (Figure 3C). To assess more
401 precisely how period changed, we calculated the peak-to-peak intervals for neuron- or astrocyte-
402 targeted SCN (Figure 3D). Again, both cell-types produced equivalent period changes (repeated
403 measures 2-way ANOVA cell-type effect, $F(1, 20) =3.43$, $p =0.08$), with significant lengthening
404 following the addition of the AAV-Cre (repeated measures 2-way ANOVA time effect, $F(4.93, 93.13)$
405 =17.17, $p<0.0001$) (Figure 3D). Consistent with the previous observation, however, there was a
406 significant difference in the temporal dynamics required to achieve this period change between the

407 two cell-types: neuron-targeted SCN lengthened period more rapidly than astrocyte-targeted SCN
408 (repeated measures 2-way ANOVA cell-type-by-time interaction, $F(21, 397) = 2.25$, $p = 0.001$) (Figure
409 3D). Having established that neurons determine period much more rapidly than do astrocytes, we
410 refined this observation by determining the number of cycles post-Cre transduction at which the peak-
411 to-peak period lengthened beyond the point of the half-maximal period change (Figure 3E).
412 Neuronally targeted SCN reached this point in about half the number of cycles that it took for
413 astrocytically targeted SCN (neurons vs. astrocytes: 2.8 ± 0.3 vs. 5.3 ± 0.6 cycles, unpaired Welch's
414 two-tailed t-test, $t(12.35) = 3.01$, $p = 0.011$) (Figure 3E). Notwithstanding the more demanding context
415 of a functional rather than circadian-incompetent SCN circuit, the relative rate of the pacemaking
416 exerted by the cell-autonomous astrocytic clock was again approximately half as fast as that of the
417 neuronal clock. TTFL-encoded timing cues from astrocytes can slow the period of the whole SCN,
418 but take longer than do neuronally derived cues. Perhaps the cues have different intrinsic potencies,
419 and/ or astrocytes are more readily controlled (slowed) by neurons, than vice versa.

420

421 From a conceptual perspective, it might be expected that slowing down circadian time-keeping, which
422 could be achieved by inhibiting a single rate-limiting process, may be easier than accelerating it,
423 which would require all processes to be regulated simultaneously. Indeed, most tests of neuronal
424 pacemaking have relied on lengthening their cell-autonomous TTFL (Lee et al., 2015; Smyllie et al.,
425 2016; Brancaccio et al., 2017; van der Vinne et al., 2018; Brancaccio et al., 2019; Patton et al., 2020;
426 Hamnett et al., 2021). As a final comparison of neuronal and astrocytic pacemaking, we therefore
427 exploited genetic complementation of *Cry2*, in either neurons or astrocytes, in order to shorten the
428 period of *Cry2*-null SCN. This would not only test the bi-directional effect of cell-autonomous neuronal
429 and astrocytic clocks, but also provide a potentially more resistant context for this comparison.
430 Bioluminescence rhythms of *Cry2*-null SCN exhibited characteristically long periods (~26 h) in the
431 presence of AAV *pCry2*-DIO.CRY2::EGFP AAV (Figure 3F). On addition of neuronally specific AAV-
432 Cre, the period progressively shortened over the subsequent 20 days (Fig. 3F, G) to 24.2 ± 0.15 h.
433 Addition of the astrocyte-specific AAV-Cre also caused period to shorten (2-way ANOVA interval
434 effect, $F(1, 12) = 85.25$, $p < 0.0001$), but the final stable period (25.01 ± 0.15 h) was significantly longer
435 than neuronally targetted SCN (Figure 3G) (2-way ANOVA cell-type effect, $F(1, 12) = 14.4$, $p = 0.003$;
436 cell-type-by-interval interaction, $F(1,12) = 9.70$, $p = 0.009$). FFT-based analysis across the experiment

437 confirmed that both populations were able to shorten period progressively (2-way ANOVA interval
438 effect, $F(3, 36) = 19.41$, $p < 0.0001$), but were not equally effective (2-way ANOVA cell-type effect, $F(1,$
439 $12) = 12.96$, $p = 0.004$; cell-type-by-interval interaction, $F(3, 36) = 6.72$, $p = 0.001$) (Figure 3H). These
440 experiments reveal, first, that the cell-autonomous clock of either neurons or astrocytes can shorten,
441 as well as lengthen, the ensemble period on the SCN, and, second, that astrocytes are much less
442 potent than neurons in this regard. In the case of lengthening period, both cell types are ultimately
443 equally effective, albeit neurons are effective sooner. With potentially more demanding period
444 shortening, although both populations can shorten period to some extent, astrocytes are much
445 weaker pacemakers than are neurons, such that the emergent ensemble period more closely
446 matches that of the period of the surrounding untargetted neurons.

447

448 ***Chemogenetic manipulation of astrocytic cellular activity***

449 Disrupting astrocytic metabolism, initiating rhythmicity de novo and changing ensemble period are
450 chronic manipulations of the ongoing SCN oscillation, but to what extent can acute changes to the
451 cellular activity of neurons and astrocytes alter the phase of SCN time-keeping? We therefore
452 expressed designer receptors exclusively activated by designer drugs (DREADDs) to manipulate
453 neurons or astrocytes chemogenetically via Gi- or Gq-coupled receptors. Chemogenetic targeting of
454 SCN neurons has been reported previously (Brancaccio et al., 2013), but to determine its efficacy in
455 SCN astrocytes, we expressed GCaMP6f under the control of the GFAP promoter to monitor
456 astrocytic $[Ca^{2+}]_i$. Using Per2::Luciferase as a circadian reference point, we re-confirmed circadian
457 oscillations of $[Ca^{2+}]_i$ in astrocytes (Fig. 4A) with the appropriate period (Per2::Luciferase, 24.4 ± 0.1 h:
458 GCaMP6f, 24.3 ± 0.1 h, $n = 11$, paired two-tailed t-test, $t(10) = 0.93$, $p = 0.37$) and a nocturnal peak
459 (CT17.6 ± 0.3 h, $n = 11$). In Cry-null SCN the rhythm of Per2::Luciferase bioluminescence was lost,
460 such that its rhythmicity index (autocorrelation at 24 h) was significantly reduced (wild-type vs. Cry-
461 null: 0.70 ± 0.02 vs. 0.03 ± 0.06 au, unpaired Welch's two-tailed t-test, $t(6.892) = 10.82$, $p < 0.0001$).
462 Equally, the circadian cycle of $[Ca^{2+}]_i$ in astrocytes was also absent in Cry-null SCN, with a reduced
463 rhythmicity index (wild-type vs. Cry-null: unpaired Welch's two-tailed t-test, $t(14.61) = 4.34$, $p = 0.0006$)
464 (Figure 4B). The astrocytic $[Ca^{2+}]_i$ rhythm is therefore dependent on the SCN TTFL. We then used
465 Cry-null SCN to assess the efficacy of acute chemogenetic manipulation of astrocytic activity,

466 reported as $[Ca^{2+}]_i$, in the absence of any confound from circadian oscillations. The Gi-coupled
467 DREADD, hM4Di, delivered to SCN astrocytes via AAV (*GFAP*-hM4Di::mCherry), exhibited
468 appropriate astrocytic distribution (Figure 4C), in close register to astrocytic GCaMP6f. On dropwise
469 addition of vehicle, astrocytic $[Ca^{2+}]_i$ fluctuated transiently, but rapidly returned to baseline levels
470 (Figure 4C). In contrast, addition of 100nM CNO rapidly elevated aggregate astrocytic $[Ca^{2+}]_i$, and
471 activated cells across the SCN; an effect that persisted for ~30 seconds before a return to baseline
472 levels (Figure 4C). Consequently, the mean $[Ca^{2+}]_i$ level over the first 30 seconds following acute
473 treatment exhibited a significant elevation, compared to vehicle (Veh vs. CNO, 0.04 ± 0.04 vs. 0.57
474 ± 0.16 au, paired two-tailed t-test $t(5) = 3.43$, $p = 0.019$) (Figure 4C). We next tested the ability of the
475 Gq-coupled DREADD, hM3Dq (*GFAP*-hM3Dq::mCherry) to manipulate astrocytic $[Ca^{2+}]_i$. Again, this
476 revealed an appropriate astrocytic distribution of mCherry fluorescence (Figure 4D) and dropwise
477 addition of vehicle caused a transient fluctuation of astrocytic $[Ca^{2+}]_i$ before it returned to baseline
478 levels (Figure 4D). In contrast, addition of 100nM CNO caused an immediate and sustained elevation
479 of astrocytic $[Ca^{2+}]_i$ (Figure 4D). Again, the mean CNO-induced elevation of astrocytic $[Ca^{2+}]_i$ over the
480 first 30 seconds of treatment was significantly elevated relative to vehicle (Veh vs. CNO, 0.11 ± 0.11
481 vs. 2.52 ± 0.78 au, paired two-tailed t-test $t(4) = 3.33$, $p = 0.03$) (Figure 4D). Thus, Gi- and Gq-coupled
482 DREADDs are functional in SCN astrocytes, and although they both trigger elevations of $[Ca^{2+}]_i$, these
483 responses are qualitatively different, indicating that Gi- and Gq-coupled DREADDs activate distinct
484 intracellular pathways in astrocytes.

485

486 ***Differential chemogenetic determination of SCN ensemble phase by neurons and astrocytes***

487 We then used chemogenetic manipulation of neurons or astrocytes to compare their relative
488 contributions to the determination of SCN ensemble phase. Due to reported off-target effects of CNO
489 treatment caused by conversion of CNO to clozapine in murine tissues (Manvich et al., 2018), we
490 assessed any non-specific effects of CNO treatment using untransduced Per2::Luciferase SCN slices
491 treated across circadian time. After baseline recording of circadian bioluminescence, SCN were
492 treated with vehicle or CNO (100 nM) in culture medium for 1 hour by transfer to a separate culture
493 dish. Following serial wash-out, the slices were returned to their original culture dish and luciferin-
494 containing medium, and recording was continued (Figure 4E). These experiments revealed that there

495 is no effect on ensemble phase when SCN explants are treated with vehicle or CNO in this way
496 (repeated measures 2-way ANOVA treatment effect, $F(1, 16) = 0.0004$, $p = 0.98$), nor was there any
497 dependence on phase of treatment (repeated measures 2-way ANOVA phase effect, $F(3, 16) = 2.10$,
498 $p = 0.14$; treatment-by-time interaction, $F(3, 16) = 0.07$, $p = 0.98$) (Figure 4F).

499

500 Having established chemogenetic manipulation of astrocytes and neurons as viable tools for studying
501 phase determination in the SCN, we first expressed the Gi-coupled DREADD (hM4Di) under the *Syn*
502 promoter in neurons of *Per2::Luciferase* SCN slices. Neuronal Gi-activation had both acute and
503 sustained effects in slices treated across circadian time (Figure 5A). The height of the first peak
504 following treatment was strongly reduced by CNO treatment (Figure 5B) (repeated measures 2-way
505 ANOVA treatment effect, $F(1, 8) = 11.37$, $p = 0.0098$), but this did not appear to be associated with the
506 phase at which treatment was given (repeated measures 2-way ANOVA phase effect, $F(3, 24) = 0.38$,
507 $p = 0.77$) nor an interaction (repeated measures 2-way ANOVA, treatment-by-phase interaction, $F(3,$
508 $12) = 2.01$, $p = 0.17$). However, looking at how this acute suppression of the peak manifested across
509 recordings, post-hoc testing revealed a specific effect when slices were treated in early circadian day,
510 CT0-6 (Šidák's multiple comparisons test: $p = 0.0027$) at a time when neuronal calcium and electrical
511 activity is rising to the peak (Colwell, 2011; Patton et al., 2020). Conversely, treatments given after
512 this time did not show the same acute suppression of the peak (Šidák's multiple comparisons test:
513 CT6-12, $p = 0.68$; CT12-18, $p = 0.57$; CT18-24, $p = 0.68$). Assessment of the acute effects on cycle
514 amplitude revealed the same pattern (Figure 5C), with CNO suppressing the amplitude of the first
515 cycle post-treatment (repeated measures 2-way ANOVA treatment effect, $F(1, 52) = 8.14$, $p = 0.0062$)
516 without revealing a phase specific or interaction effect (repeated measures 2-way ANOVA phase
517 effect, $F(3, 52) = 0.81$, $p = 0.5$; treatment-by-phase interaction, $F(3, 52) = 0.87$, $p = 0.5$). Again, post-
518 hoc tests revealed that this change in peak amplitude manifested as a suppression specifically during
519 early circadian day, CT0-6 (Šidák's multiple comparisons test: $p = 0.04$) without effect at other phases
520 (Šidák's multiple comparisons test: CT6-12: $p = 0.29$; CT12-18: $p = 0.9$; CT18-24: $p = 0.96$).

521

522 We then assessed the sustained effects of neuronal chemogenetic inhibition on ensemble phase.
523 Although the treatment effect did not reach significance (repeated measures 2-way ANOVA treatment

524 effect, $F(1, 8) = 2.91$, $p = 0.13$), consistent with the acute effects we saw at CT0-6, there was a
525 significant effect of phase of treatment (repeated measures 2-way ANOVA phase effect $F(3, 24)$
526 $= 4.23$, $p = 0.016$). However, the interaction between phase and treatment failed to reach significance
527 (repeated measures 2-way ANOVA phase-by-treatment interaction, $F(3, 12) = 3.33$, $p = 0.057$).
528 Further examination of the phase-specific effect revealed that, again, consistent with the acute effects
529 on amplitude, chemogenetic manipulation during the early circadian day, CT0-6, elicited a significant
530 phase advance (Šidák's multiple comparisons test: $p = 0.019$), whereas treatment at later phases was
531 without effect (Šidák's multiple comparisons test: CT6-12: $p = 0.45$; CT12-18: $p > 0.99$; CT18-24: p
532 $= 0.80$).

533

534 We then assessed the effects of Gi activation in astrocytes (Figs 5E-H). The height of the first peak
535 following chemogenetic manipulation was not significantly altered by treatment with CNO (repeated
536 measures two-way ANOVA treatment effect, $F(1, 6) = 5.16$, $p = 0.064$), but was associated with a
537 phase dependent effect (repeated measures 2-way ANOVA phase effect, $F(3, 18) = 4.38$, $p = 0.018$).
538 Despite this, there was no interaction between phase and treatment (repeated measures 2-way
539 ANOVA phase-by-treatment interaction, $F(3, 6) = 2.23$, $p = 0.19$). We therefore investigated the phase
540 dependent effect further by post-hoc multiple comparisons testing, and saw that there was a
541 significant effect of treatment with CNO during the middle of circadian day, CT6-12 (Šidák's multiple
542 comparisons test: $p = 0.04$), but no effect at any other phase (Šidák's multiple comparisons test: CT0-
543 6, $p > 0.99$; CT12-18, $p = 0.27$; CT18-24, $p > 0.99$) (Figure 5F) leading us to conclude that the phase
544 dependence arises due to a small suppression of the peak amplitude when astrocytes are acutely
545 manipulated during late circadian day: a phase at which their $[Ca^{2+}]_i$ is rising (Figure 4A) (Brancaccio
546 et al., 2017) and at which fluorocitrate treatment is most acutely effective (Figure 1H). This further
547 confirmed efficacy on the Gi activation in astrocytes, consistent with our calcium data (Figure 4D, E).
548 Despite this observation, there was no significant effect of phase (repeated measures 2-way ANOVA
549 phase effect, $F(3, 18) = 2.23$, $p = 0.12$), of treatment (repeated measures 2-way ANOVA treatment
550 effect, $F(1, 6) = 4.34$, $p = 0.08$) or interaction (repeated measures 2-way ANOVA phase-by-treatment
551 interaction, $F(3, 6) = 0.93$, $p = 0.48$) when we assessed the acute effects on cycle amplitude (Figure
552 5G).

553

554 Having established this weak acute effect of astrocytic Gi-coupled signalling on TTFL waveform, we
555 then determined whether there was a sustained effect on ensemble phase (Figure 5H). This revealed
556 no significant effect of phase (repeated measures 2-way ANOVA phase effect, $F(3, 18) = 2.89$, p
557 $= 0.064$), of treatment (repeated measures 2-way ANOVA treatment effect, $F(1, 6) = 3.03$, $p = 0.13$) or
558 interaction between phase and treatment (repeated measures 2-way ANOVA phase-by-treatment
559 effect, $F(3, 6) = 0.22$, $p = 0.88$) (Figure 5H). These data reveal, therefore, that chemogenetic inhibition
560 of neurons can strongly advance the phase of the ensemble circadian oscillation in a phase-
561 dependent manner, associated with an acute reduction in the amplitude of the following cycle. In
562 contrast, the same manipulation in astrocytes does not induce a phase shift at any phase of the
563 circadian oscillation, nor does it acutely alter the waveform following treatment although it may weakly
564 disrupt the peak following treatment. Thus, neuronal Gi-signalling revealed effective control of SCN
565 phase by neurons, but regulation of Gi signals in astrocytes was without long-term effect.

566

567 We then used Gq-DREADD to activate $[Ca^{2+}]_i$, first in neurons, recording any acute or sustained
568 effects on the rhythm of Per2::Luciferase activity of SCN slices (Figure 6A-D). The height of the first
569 peak following treatment was enhanced, manifesting as significant effects of phase (repeated
570 measures 2-way ANOVA phase effect, $F(3, 25) = 5.92$, $p = 0.003$), of treatment (repeated measures 2-
571 way ANOVA treatment effect, $F(1, 25) = 63.48$, $p < 0.0001$) and as an interaction between phase and
572 treatment (repeated measures 2-way ANOVA phase-by-treatment interaction, $F(3, 25) = 5.18$, p
573 $= 0.006$). Post-hoc multiple comparisons revealed that these effects were caused by an acute
574 increase in the height of the first peak after treatment during the circadian day or the late circadian
575 night (Šidák's multiple comparisons test: CT0-6, $p < 0.0001$; CT6-12, $p = 0.006$; CT18-24, $p < 0.0001$)
576 but not during the early circadian night (Šidák's multiple comparisons test: CT12-18, $p = 0.77$) (Figure
577 6B). We further examined the acute effects on cycle amplitude following treatment, expecting this to
578 follow suit as with the neuronal Gi-signalling (Figure 5B, C). Assessing cycle amplitude, we saw that
579 there was a significant effect of phase (repeated measures 2-way ANOVA phase effect, $F(3, 25)$
580 $= 10.23$, $p = 0.0001$) but no significant effect of treatment (repeated measures 2-way ANOVA treatment
581 effect, $F(1, 25) = 0.02$, $p = 0.88$). There was, however, a significant interaction between phase and

582 treatment (repeated measures 2-way ANOVA phase-by-treatment interaction, $F(3, 25) = 10.6$, p
583 $= 0.0001$). We therefore investigated the phase specific effects via post-hoc multiple comparisons,
584 revealing a complex phenotype whereby cycle amplitude remained unchanged after treatment in
585 circadian day (Šidák's multiple comparisons test: CT0-6, $p > 0.99$; CT6-12, $p = 0.54$), but was reduced
586 during early circadian night, CT12-18 ($p = 0.0006$) and this increased during late circadian night,
587 CT18-24 (Šidák's multiple comparisons test: $p = 0.018$). These changes can be attributed to a
588 combination of the previously described peak changes (Figure 6B) and an increased baseline (Figure
589 6A), a well characterised feature of neuronal Gq-manipulation in SCN slices presumed to be acting
590 through the VIP signalling axis (Branaccio et al., 2013; Hamnett et al., 2019). The potent acute
591 effects of Gq-activation in neurons were reflected in sustained effects on ensemble phase (Figure
592 6D), which revealed a significant effect of treatment (repeated measures 2-way ANOVA treatment
593 effect, $F(1, 50) = 8.10$, $p = 0.006$). Although there was no overall effect of phase (repeated measures
594 2-way ANOVA phase effect, $F(3, 50) = 2.40$, $p = 0.08$) there was a significant interaction between
595 phase and treatment (repeated measures 2-way ANOVA phase-by-treatment interaction, $F(3, 50)$
596 $= 2.98$, $p = 0.040$). Post-hoc comparisons revealed a significant phase delay when slices were treated
597 during circadian day (Šidák's multiple comparisons test: CT0-6, $p = 0.023$; CT6-12, $p = 0.028$) but no
598 phase shift when slices were treated during circadian night (Šidák's multiple comparisons test: CT12-
599 18, $p < 0.99$; CT18-24, $p < 0.99$). Gq-coupled manipulation of neurons therefore altered TTFL waveform
600 in a phase-dependent manner and strongly reset ensemble phase.

601

602 We then assessed the acute and sustained effects of Gq-manipulation in astrocytes (Figure 6E). The
603 amplitude of the first peak of Per2::Luciferase following treatment (Figure 6F) did not show any
604 significant effect of treatment (repeated measures 2-way ANOVA, treatment effect, $F(1, 9) = 0.01$, p
605 $= 0.95$) or phase (repeated measures 2-way ANOVA phase effect, $F(3, 27) = 0.47$, $p = 0.71$), nor an
606 interaction between the two (repeated measures 2-way ANOVA, phase-by-treatment interaction, $F(3,$
607 $3) = 0.36$, $p = 0.79$). We then assessed the acute effects on cycle amplitude, and again there were no
608 significant effects of treatment (repeated measures 2-way ANOVA, treatment effect, $F(1, 9) = 0.63$, p
609 $= 0.44$) or phase (repeated measures 2-way ANOVA, phase effect, $F(3, 27) = 0.28$, $p = 0.84$), or any
610 interaction (repeated measures 2-way ANOVA, phase-by-treatment interaction, $F(3, 3) = 0.66$, p
611 $= 0.63$) (Figure 6G). Thus, manipulation of astrocytic Gq-signalling pathways did not acutely alter the

612 waveform of SCN ensemble molecular timekeeping. We then assessed whether the direct
613 manipulation of Gq in astrocytes could reset ensemble phase (Figure 6H). This revealed no
614 significant effect of treatment itself (repeated measures 2-way ANOVA, treatment effect, $F(1, 9)$
615 =3.37, $p = 0.10$), although there was a significant effect of phase of treatment (repeated measures 2-
616 way ANOVA, phase effect, $F(3, 27) = 5.39$, $p = 0.005$), but no interaction between phase and treatment
617 (repeated measures 2-way ANOVA, phase-by-treatment interaction, $F(3, 3) = 3.12$, $p = 0.19$). Multiple
618 post-hoc comparisons of the phase main effect revealed no significant differences between CNO and
619 vehicle treatment at any phase (Šidák's multiple comparisons test: CT0-6, $p > 0.99$; CT6-12, $p = 0.09$;
620 CT12-18, $p = 0.29$; CT18-24, $p = 0.80$). We therefore concluded that the phase-dependence largely
621 arose from fluctuations due to the experimental protocol and not from a sustained phase-shift induced
622 by activation of Gq in astrocytes. Thus, TTFL phase in the SCN is acutely sensitive to activation of
623 both Gi- and Gq-coupled pathways in neurons, but not in astrocytes. Taken together, these
624 experiments reveal important differences between the contributions made by astrocytes and neurons
625 in regulating the emergent properties of the SCN circadian network. Whereas ensemble phase is bi-
626 directionally sensitive to neuronal activity, it is not affected by chemogenetic stimulation of astrocytes.
627 In contrast, astrocytes play important roles in maintaining the properties of the ongoing SCN
628 oscillation: its amplitude, inter-cellular synchrony and ensemble period.

629

630

631 **Discussion**

632 SCN astrocytes display circadian TTFL and $[Ca^{2+}]_i$ rhythms in stable anti-phase to those of SCN
633 neurons (Brancaccio et al., 2017; Tso et al., 2017; Brancaccio et al., 2019). This implies that strong
634 coupling signals between their respective TTFLs sustain and organise network-wide oscillations,
635 (Hastings et al., 2018). Consistent with this, chronic treatment of SCN slices with the metabolic
636 gliotoxin fluorocitrate which disrupted astrocytic $[Ca^{2+}]_i$ oscillations also suppressed the amplitude of
637 the ongoing ensemble neuronal TTFL (Per2::Luciferase) oscillation. Metabolic compromise of
638 astrocytes also impaired cellular synchrony, indicative of looser network coupling: a phenotype more
639 commonly associated with compromised neuronal signalling (Figure 1) (Yamaguchi et al., 2003;
640 Maywood et al., 2006). Importantly, the immediate effect of fluorocitrate was phase-dependent, being
641 evident between CT06-18: the rising phase of astrocytic activation. Conversely, application during
642 declining astrocytic activity (CT18-06), saw the effect on the TTFL delayed to the next cycle,
643 consistent with a phase-restricted contribution of astrocytes to network function. This result extends
644 the report that fluorocitrate applied at CT06 to acutely prepared rat SCN slices disrupted neuronal
645 electrical activity rhythms on the following cycle (Prosser et al., 1994). Given that SCN firing and
646 TTFL function are intimately linked (Colwell, 2011), it remains to be determined which of them is the
647 primary target of astrocytic signals. Thus, astrocytes reinforce SCN neuronal rhythmicity, potentially
648 through appropriate inhibition of neuronal electrical activity during circadian night when astrocytes are
649 most active. Although the metabolically sensitive astrocytic signal(s) awaits identification, it may
650 involve astrocytic glutamate release, which is sensed by pre-synaptic neuronal NR2C receptors,
651 (Brancaccio et al., 2017). Consistent with this model, fluorocitrate inhibits glutamate and glutamine
652 synthesis from radiolabelled glucose in cultured cortical and cerebellar astrocytes (Hassel et al.,
653 1995), while inhibition of NR2C-signalling suppresses the amplitude of SCN Per2::Luciferase
654 oscillations, similar to fluorocitrate treatment (Brancaccio et al., 2017). Additionally, astrocyte-
655 mediated active uptake of GABA (Barca-Mayo et al., 2017) or an endocannabinoid/adenosine
656 signalling axis (Hablitz et al., 2020) may also control neuronal rhythms.

657

658 The potency of astrocytic signals was most evident in the initiation of rhythmic Per2 expression in Cry-
659 null SCN (Figure 2), occurring alongside de novo neuronal $[Ca^{2+}]_i$ rhythms (Brancaccio et al., 2019).

660 The latter may involve calcium-dependent cytosolic signalling pathways impinging on *Period* gene
661 expression (Travnickova-Bendova et al., 2002), and/or CHRONO or DEC1/2 proteins compensating
662 for the absence of Cry proteins (Ono et al., 2021). Such indirect, paracrine astrocytic control of
663 neuronal TTFLs may explain why genetic complementation of Cry in astrocytes takes longer to initiate
664 or amend the network period than does neuronal complementation. During the lag, it is possible that
665 progressive mutual reinforcement between initially weak astrocytic TTFLs (Prolo et al., 2005) and
666 defective Cry-null neuronal clocks leads to an iterative auto-amplification of astrocyte-to-neuron and
667 neuron-to-astrocyte signals, slowing building ensemble TTFL amplitude. As SCN neurons are
668 enriched for neuropeptide expression (Morris et al., 2021), these molecules might modulate neuronal
669 feedback to SCN astrocytes. Indeed, the SCN-enriched neuropeptide VIP has been implicated as an
670 entraining and synchronising factor for astrocytic circadian rhythms (Prolo et al., 2005; Marpegan et
671 al., 2009; Sueviriyapan et al., 2020). Importantly, the end-point oscillations maintained by astrocytes
672 are indistinguishable from neuronally driven oscillations.

673

674 Astrocytes, as well as neurons, slowed SCN rhythms to match the period of their cell-autonomous
675 TTFL, (Figure 3) with SCN period reflected at the behavioural level (Brancaccio et al., 2017; Tso et
676 al., 2017; Brancaccio et al., 2019). Again, astrocytes took longer to achieve this (Figure 3).
677 Nevertheless, Cry1-expressing astrocytes were effective and, indeed, when SCN astrocytes lack a
678 functional molecular clock, following BMAL1 deletion, they can also slow down the circadian
679 oscillation at the network and the behavioural levels (Barca-Mayo et al., 2017; Tso et al., 2017). A
680 more dramatic difference between neurons and astrocytes came, however, with acceleration of TTFL
681 rhythms by Cry2 complementation of Cry2-null SCN. Neurons shortened SCN ensemble period by
682 ~1.5 h, to match their cell-autonomous period, confirming their role as strong pacemakers through bi-
683 directional control of the ongoing oscillation. The effect of accelerating the cell-autonomous period of
684 SCN astrocytes, however, was a marginal shortening of ~0.4 h. This confirms their bi-directional
685 influence, but also highlights their junior role relative to neurons. Conceptually, slowing down
686 circadian time-keeping (which could be achieved by inhibiting a single rate-limiting process) may be
687 easier than accelerating it, which would require simultaneous regulation of all processes. Thus,

688 indirect, likely inhibitory signals from astrocytes are less effective at the circuit level than is direct
689 manipulation of the neuronal TTFL.

690

691 We observed differences between astrocytes and neurons in their cellular response to DREADD
692 activation. Whereas activation of Gi- (hM4Di) or Gq-coupled (hM3Dq) DREADDs achieved inhibition
693 and excitation of neuronal activity, respectively (Roth, 2016), in astrocytes, activation of either
694 DREADD subtype triggered rises in $[Ca^{2+}]_i$ (Figure 4) (Yu et al., 2020; Shen et al., 2021), albeit with
695 qualitative differences. Consistent with dorsal striatum and hippocampus (Chai et al., 2017; Durkee et
696 al., 2019; Nagai et al., 2019), Gi-activation in SCN astrocytes caused a small, rapid calcium increase,
697 although somatic localisation of the reporter means we cannot exclude larger changes occurring at
698 distal membrane processes (Semyanov et al., 2020). In contrast, Gq-coupled signalling in astrocytes
699 caused large, prolonged rises across the astrocytic network, consistent with responses in the
700 amygdala (Martin-Fernandez et al., 2017) and hippocampus (Chai et al., 2017; Adamsky et al., 2018;
701 Durkee et al., 2019). Despite these rises indicating astrocytic activation under cell-type-specific Gq-
702 manipulation, interpretation of the effect on astrocytic activity may be more complex than anticipated:
703 Gq-activation in cortical astrocytes leads to long-term cessation of calcium spiking despite an
704 elevated baseline. This points towards some level of astrocytic silencing (Vaidyanathan et al., 2021).
705 It is therefore imperative to understand how astrocytic activity encodes circadian time, and whether it
706 is calcium spiking, bulk calcium or both that are responsible for astrocytic information transfer to the
707 rest of the network. Nevertheless, these observations confirmed chemogenetic manipulation as a
708 useful tool to control astrocytic calcium signalling in the SCN (Semyanov et al., 2020).

709

710 Chemogenetic activation of SCN neurons caused acute phase-dependent differences in
711 Per2::Luciferase expression: suppression by Gi and elevation by Gq. These were accompanied by
712 phase shifts: advances and delays, respectively and are consistent, respectively, with behaviourally
713 induced non-photic resetting by inhibition of SCN neural activity (Gribkoff et al., 1998; Maywood et al.,
714 1999; Jones et al., 2015), and photic resetting by retinally mediated activation of SCN neurons
715 (Shearman et al., 1997; Meijer and Schwartz, 2003; Jones et al., 2015). In contrast, direct

716 chemogenetic activation of Gi or Gq in astrocytes did not affect phase of the ongoing SCN oscillation
717 (Figures 5 and 6). This observation may be at odds with reports that astrocytes can modulate phase
718 advances in early circadian day in SCN explants via a neuron-to-astrocyte signalling pathway where
719 cannabinoid receptors enhance astrocytic adenosine release (Hablitz et al., 2020). It is likely,
720 therefore, that where SCN astrocytes can modulate phase shifts, they actually mediate a neuronal
721 effect, so their direct activation alone, as presented here, is not sufficient to reset ensemble phase.
722 These differences may reflect SCN cellular architecture – the neuronal network receives strong
723 synaptic inputs, for example from the retinal hypothalamic tract, intergeniculate leaflet and midbrain
724 raphe (Morin and Allen, 2006), allowing it to respond rapidly to afferent entraining signals. Astrocytes,
725 in contrast, do not receive these signals. Rather, they likely receive input from paracrine sources and
726 via their integration within tripartite synapses (Perea et al., 2009), where they modulate and integrate
727 synaptic communication. It is therefore conceivable that SCN astrocytes modulate the response of
728 the SCN network to afferent signals or influence SCN output in intact animals, whereas by performing
729 these experiments in SCN explants the manipulation is without effect. It remains to be determined
730 whether chemogenetic manipulation of astrocytes has any effects *in vivo*.

731 A final consideration is that SCN neurons outnumber SCN astrocytes by a factor of 3 to 1 (Guldner,
732 1983). However, individual astrocytes have been reported to contact up to 100,000 synapses
733 (Halassa et al., 2007) whereas SCN neurons make up to an estimated 1000 synaptic contacts each
734 (Moore and Bernstein, 1989). Despite their lower abundance, therefore, the astrocytic area of pan-
735 network influence may be similar to, or greater than, that of neurons. Furthermore, experiments
736 conditionally targeting SCN neuronal populations have revealed that a similar proportion of neurons:
737 those expressing the VIP receptor, VPAC2 (Patton et al., 2020; Morris et al., 2021) cannot set
738 ensemble phase, lengthen period or initiate *de novo* rhythmicity by *Cry1* complementation alone
739 (Patton et al., 2020). In contrast, Cre-conditional *Bmal1* ablation targeted to astrocytes (Barca-Mayo
740 et al., 2017; Tso et al., 2017) or AVP-neurons (Mieda et al., 2015; Shan et al., 2020) lengthens
741 behavioural period, which only persists in the SCN explant when astrocytes are targeted. Taken
742 together, these results suggest that at some level of SCN network computation, astrocytes transfer
743 certain types of circadian information more potently than defined neuronal populations. Thus,
744 understanding the cellular roles and architecture of the SCN astrocyte-neuron network is paramount
745 in understanding how the SCN generates and disseminates time-of-day information.

747 **Acknowledgements**

748 This work was funded by MRC core funding (MC_U105170643) and the BBSRC grant award
749 (BB/R016658/1). The Authors are grateful for excellent technical support from MRC Biomedical
750 Facility (Ares) and the LMB Electronic and Mechanical Workshops.

751

752 **Author Contributions**

753 A.P.P and M.H.H designed the research and wrote the manuscript. A.P.P performed the
754 experiments. N.J.S. developed novel reagents. J.E.C. supervised animal husbandry.

755 **Figure Legends**

756

757 **Figure 1: Astrocytic metabolic competence is required for robust, high amplitude SCN**
758 **oscillation.**

759 **A.** Example astrocytic calcium rhythms (*GFAP*-cytoCaMP6f) from slices treated with vehicle (left) or
760 50 μ M fluorocitrate (right) expressed as relative amplitude. Shading indicates the interval of chronic
761 treatment with either vehicle (grey) or 50 μ M fluorocitrate (teal). **B.** Histogram showing paired peak-
762 to-trough amplitude measures of the first cycle of the aggregate calcium rhythm under either vehicle
763 (grey, N=4) or 50 μ M fluorocitrate (teal, N=4) treatment normalised to the peak-to-trough amplitude of
764 the cycle preceding treatment. Statistics: Paired two-tailed t-test, *p =0.018. **C.** Example normalised
765 PMT traces of aggregate *Per2::Luciferase* bioluminescent signals showing effects of treating SCN
766 slices with vehicle (left) or 50 μ M fluorocitrate (middle, right). Shading indicates the interval of chronic
767 treatment with either vehicle (grey) or 50 μ M fluorocitrate (teal). **D.** Histogram showing period change
768 in hours from baseline, of *Per2::Luciferase* rhythms induced by treatment with vehicle (Veh. grey,
769 N=19) or 50 μ M fluorocitrate (FC, teal, N=22). **E.** Histogram showing the change in RAE ratio
770 (treatment/baseline) of *Per2::Luciferase* rhythms for vehicle (Veh, grey, N=19) and 50 μ M fluorocitrate
771 (FC, teal, N=22) treated slices. **F.** Histogram showing the normalised amplitude of *Per2::luciferase*
772 rhythms expressed as the amplitude of the treatment interval normalised to the amplitude of the
773 baseline interval for vehicle (Veh, grey, N=19) and 50 μ M fluorocitrate (FC, teal, N=22) treated slices.
774 Statistics: unpaired two-tailed Welch's t-test, ****p<0.0001. **G.** Cycle-to-cycle amplitude of the
775 *Per2::Luciferase* rhythm normalised to the peak post-treatment for vehicle (Veh, grey, N=19) and
776 50 μ M fluorocitrate (FC, teal, N=22) treated slices. Each point represents the mean \pm SEM. Statistics:
777 post-hoc Šidák's multiple comparisons, ****p<0.0001. **H.** Histogram showing the amplitude of the
778 first *Per2::Luciferase* peak of the treatment interval normalised to the last *Per2::Luciferase* peak of the
779 baseline interval for vehicle (grey) and 50 μ M fluorocitrate (teal) treated slices, separated by phase of
780 treatment. N \geq 4 for each phase. Statistics: Šidák's multiple comparisons, *p =0.031, **p =0.002. **I.**
781 False-coloured raster plot showing *Per2::Luciferase* bioluminescence from individual oscillators
782 across the SCN network through time under 50 μ M fluorocitrate treatment recorded via CCD camera.
783 Treatment interval is indicated by the teal bar. **J.** Histogram showing normalised amplitude of

784 aggregate Per2::Luciferase bioluminescence rhythms expressed as the amplitude of the treatment
785 interval normalised to the amplitude of the baseline interval of vehicle (Veh, grey, N=7) and 50µM
786 fluorocitrate (FC, teal, N=7) treated slices. Paired recordings under vehicle or 50µM fluorocitrate are
787 indicated by lines connecting individual points. Statistics: paired two-tailed t-test, ***p=0.0003. **K.**
788 Histogram showing Rayleigh vector length determined from network-wide cellular Per2::Luciferase
789 emissions during baseline (hollow bars, BL) or treatment (solid bars, TR) intervals. Vehicle treatment
790 (N=7) is indicated by grey colouration and 50µM fluorocitrate treatment (N=7) is indicated by teal
791 colouration. Statistics: Šidák's multiple comparisons, *p =0.011, **p =0.006. In all histogram plots,
792 individual points represent individual slices (with instances where data are paired being joined by lines
793 aside from **K** where pairing is not shown for clarity), and histogram bars with error bars represent
794 mean ± SEM.
795

796 **Figure 2: Neurons and astrocytes initiate *de novo* rhythmicity in the SCN at different rates.**

797 **A.** Example PMT traces showing progression of the experiment for Cry-null SCN transduced with
798 *Syn*-mCherry::Cre (left, blue) and *GFAP*-mCherry::Cre (right, pink). Medium changes preceding AAV
799 transduction are shown by shaded grey areas. AAV transductions and medium changes following the
800 serial transduction are indicated by coloured bars (from left to right): AAV1 (*pCry1*-DIO.Cry1::EGFP,
801 green), AAV2 (*Syn*-mCherry::Cre, blue or *GFAP*-mCherry::Cre, pink), and MC1 and MC2 (medium
802 changes, grey). **B.** Histogram showing rhythmicity index for the non-initiated baseline interval (BL)
803 and the initiated slices in the final interval of the experiment (MC2) for *Syn*-mCherry::Cre (*Syn*, blue,
804 N=10) and *GFAP*-mCherry::Cre (*GFAP*, pink, N=10). Statistics: Šidák's multiple comparisons,
805 **** $p < 0.0001$. **C.** Histograms showing final initiated periods for neuron- (*Syn*, blue, N=10) and
806 astrocyte- (*GFAP*, pink, N=10) initiated SCN slices. **D.** Summary FFT-determined period data,
807 showing SCN slices transduced with *Syn*-mCherry::Cre (*Syn*, blue, N=10) or *GFAP*-mCherry::Cre
808 (*GFAP*, pink, N=10). Intervals plotted along the x-axis correspond to the experimental intervals. **E.**
809 Summary FFT-determined RAE measures, showing *Syn*-mCherry::Cre (*Syn*, blue, N=10) and *GFAP*-
810 mCherry::Cre (*GFAP*, pink, N=10). Intervals plotted along the x-axis correspond to the experimental
811 intervals. Statistics: Dunnett's multiple comparisons: neurons: ** $p < 0.01$ versus BL; astrocytes: ## p
812 = 0.004 versus BL. **F.** Histogram showing the time in hours post-transduction with the AAV-Cre to
813 initiation of rhythmicity as determined by wavelet-based analysis for *Syn*-mCherry::Cre (*Syn*, blue,
814 N=10) and *GFAP*-mCherry::Cre (*GFAP*, pink, N=10). Statistics: unpaired Welch's t-test, $p = 0.03$. **G.**
815 Example images from SCN slices transduced with *EF1a*.DIO.EYFP pre- or 5 days post-transduction
816 with either *Syn*-mCherry::Cre (left, blue) or *GFAP*-mCherry::Cre (right, pink). Scale bar = 250 μ m. **H.**
817 Aggregate time-course of normalised fluorescence intensity over 5 days post AAV-Cre transductions
818 for *Syn*-mCherry::Cre (*Syn*, blue, N=4) and *GFAP*-mCherry::Cre (*GFAP*, pink, N=4). Dashed line
819 indicates 10% increase in intensity threshold. **I.** Histogram showing the time post-transduction for the
820 normalised fluorescence intensity to pass the 10% threshold for *Syn*-mCherry::Cre (*Syn*, blue, N=4)
821 and *GFAP*-mCherry::Cre (*GFAP*, pink, N=4). In all plots, individual points indicate individual SCN with
822 instances where data are paired being connected by lines. In **D** and **E** the points represent mean
823 \pm SEM. In all plots, lines with shading enclosed by dashed lines, and histogram bars with error bars
824 represent mean \pm SEM.

825

826 **Figure 3: Neurons are more potent SCN pacemakers than astrocytes.**

827 **A.** Example PMT traces showing progression of the experiment for Cry1-null SCN transduced with
828 *Syn*-mCherry::Cre (left, blue) and *GFAP*-mCherry::Cre (right, pink). Medium changes preceding AAV
829 transduction are shown by shaded grey areas. AAV transductions and medium changes following the
830 serial transduction are indicated by coloured bars (from left to right): AAV1 (*pCry1*-DIO.CRY1::EGFP,
831 green), AAV2 (*Syn*-mCherry::Cre, blue or *GFAP*-mCherry::Cre, pink), and MC1 and MC2 (medium
832 changes, grey). **B.** Histogram showing paired first interval (AAV1) and final post-Cre interval (MC2)
833 periods for neurons (*Syn*, blue, N=11) and astrocytes (*GFAP*, pink, N=11). Statistics: Šidák's multiple
834 comparisons, *** $p < 0.001$. **C.** Summary period data for SCN slices transduced with *Syn*-
835 mCherry::Cre (*Syn*, blue, N=11) or *GFAP*-mCherry::Cre (*GFAP*, pink, N=11). Intervals plotted along
836 the x-axis correspond to the experimental intervals. Statistics: Šidák's multiple comparisons, ** p
837 =0.002 *Syn* versus *GFAP*. **D.** Summary peak-to-peak period data, showing SCN slices transduced
838 with *Syn*-mCherry::Cre (*Syn*, blue, N=11) or *GFAP*-mCherry::Cre (*GFAP*, pink, N=11). Statistics:
839 Šidák's multiple comparisons, * $p = 0.049$, ** $p = 0.001$ *Syn* versus *GFAP*. **E.** Histogram showing the
840 number of cycles post-transduction with either *Syn*-mCherry::Cre (*Syn*, blue, N=11) or *GFAP*-
841 mCherry::Cre (*GFAP*, pink, N=11) for slices to achieve the half maximal period change. Statistics:
842 unpaired Welch's t-test, * $p = 0.011$. **F.** Example PMT traces showing progression of the experiment
843 for Cry2-null SCN transduced with *Syn*-mCherry::Cre (left, blue) and *GFAP*-mCherry::Cre (right, pink).
844 Medium changes preceding AAV transduction are shown by shaded grey areas. AAV transductions
845 and medium changes following the serial transduction are indicated by coloured bars (from left to
846 right): AAV1 (*pCry2*-DIO.CRY2::EGFP, green), AAV2 (*Syn*-mCherry::Cre, blue or *GFAP*-
847 mCherry::Cre, pink), and MC1 and MC2 (medium changes, grey). **G.** Histogram showing paired
848 baseline (BL) and final post-Cre (MC2) periods for neurons (*Syn*, blue, N=7) and astrocytes (*GFAP*,
849 pink, N=7). Statistics: Šidák's multiple comparisons, ** $p = 0.002$, **** $p < 0.0001$. **H.** Summary period
850 data for SCN slices transduced with *Syn*-mCherry::Cre (*Syn*, blue, N=7) or *GFAP*-mCherry::Cre
851 (*GFAP*, pink, N=7). Intervals plotted along the x-axis correspond to the experimental intervals.
852 Statistics: Šidák's multiple comparisons, *** $p < 0.001$ *Syn* versus *GFAP*. In all histogram plots,
853 individual points represent individual slices (with instances where data are paired being joined by
854 lines), and histogram bars with error bars represent mean \pm SEM. In **C**, **D**, and **H** points are mean
855 \pm SEM.

857 **Figure 4: Acute activation of DREADDs in astrocytes triggers astrocytic calcium responses.**

858 **A.** Example traces showing PER2::LUC bioluminescence (purple) and *GFAP*-cytoGCaMP6f
859 fluorescence (green) from a wild-type (*Cry1,2^{+/+}*, left) and two *Cry*-null (*Cry1,2^{-/-}*, middle and right)
860 SCN. **B.** Histogram showing the rhythmicity index for PER2::Luciferase bioluminescence (purple)
861 and *GFAP*-cytoGCaMP6f (green) from wild-type (*Cry1,2^{+/+}*, N=11) or *Cry*-null (*Cry1,2^{-/-}*, N=7) SCN.
862 Statistics: Šidák's multiple comparisons, ***p =0.0002, ****p<0.0001. **C.** (Left panel) Example false-
863 coloured image showing astrocytic hM4Di::mCherry expression (*GFAP*-hM4Di::mCherry). (Middle
864 panel) Aggregate GCaMP6f fluorescence change from SCN slices expressing astrocytic hM4Di
865 following either vehicle (Veh, grey, N=6) or 100nM CNO (CNO, pink, N=6) treatment expressed as (F-
866 F₀)/F₀. Scale bar =250µm. (Right panel) Histogram showing the mean fluorescence change over the
867 first 30 seconds of aggregate GCaMP fluorescence following either vehicle (Veh, grey, N=6) or
868 100nM CNO (CNO, pink, N=6) treatment. Statistics: paired two-tailed t-test, *p =0.019. **D.** (Left
869 panel) Example false-coloured image showing astrocytic hM3Dq::mCherry expression (*GFAP*-
870 hM3Dq::mCherry). Scale bar =250µm. (Middle panel) Aggregate GCaMP6f fluorescence change
871 from SCN slices expressing astrocytic hM3Dq following either vehicle (Veh, grey, N=4) or 100nM
872 CNO (CNO, pink, right, N=4) treatment expressed as (F-F₀)/F₀. (Right panel) Histogram showing the
873 mean fluorescence change of aggregate GCaMP fluorescence over the first 30 seconds following
874 either vehicle (Veh, grey, N=4) or CNO (CNO, pink, N=4) treatment. Statistics: paired two-tailed t-
875 test, *p =0.03. **E.** Representative PMT traces showing acute vehicle (left) and 100nM CNO (right)
876 treatment during the CT0-6 time-window. The treatment interval is shown as a vertical line and
877 coloured according to treatment: vehicle (grey) or CNO (black). **F.** Summary phase-shift data
878 arranged by phase window of treatment showing paired recordings at that phase window for
879 untransduced SCN explants treated with vehicle (grey, N=5 at each phase) or 100nM CNO
880 (black/white, N=5 at each phase). In all plots, lines with shading encased by dashed lines represent
881 mean ±SEM, individual points represent independent slices, and histogram bars with error bars
882 represent mean ±SEM. In **C**, **D** and **F**, joined points represent paired measures.

883

884 **Figure 5: Chemogenetic activation of a Gi-coupled pathway in neurons, but not astrocytes,**
885 **resets SCN ensemble phase.**

886 **A.** Schematic showing cell-type-specific targeting of Gi-coupled DREADDs to neurons (*Syn-*
887 *hM4Di::mCherry*), but not astrocytes in the intact SCN network (left) alongside representative PMT
888 traces showing acute vehicle (middle) and 100nM CNO (right) treatment during the CT0-6 time
889 window. The treatment interval is shown as a vertical line and coloured according to treatment:
890 vehicle (grey) or CNO (blue). **B.** Summary peak amplitude data arranged by phase window of
891 treatment showing paired recordings at that window for SCN with neuronally expressed Gi-coupled
892 DREADDs treated with vehicle (grey, $N \geq 6$ at each phase) or 100nM CNO (blue, $N \geq 6$ at each phase).
893 Statistics: Šidák's multiple comparisons, $**p = 0.0027$. **C.** Summary cycle amplitude data arranged by
894 phase window of treatment showing paired recordings at that window for SCN with neuronally
895 expressed Gi-coupled DREADDs treated with vehicle (grey, $N \geq 6$ at each phase) or 100nM CNO
896 (blue, $N \geq 6$ at each phase). Statistics: Šidák's multiple comparisons, $*p = 0.0421$. **D.** Summary
897 phase-shift data arranged by phase window of treatment showing paired recordings at that phase
898 window for SCN with neuronally expressed Gi-coupled DREADDs treated with vehicle (grey, $N \geq 6$ at
899 each phase) or 100nM CNO (blue, $N \geq 6$ at each phase). Statistics: Šidák's multiple comparisons, $*p$
900 $= 0.019$. **E.** Schematic showing cell-type-specific targeting of Gi-coupled DREADDs to astrocytes
901 (*GFAP-hM4Di::mCherry*), but not neurons in the intact SCN network (left) alongside representative
902 PMT traces showing acute vehicle (middle) and 100nM CNO (right) treatment during the CT0-6 time
903 window. The treatment interval is shown as a vertical line and coloured according to treatment:
904 vehicle (grey) or CNO (pink). **F.** Summary peak amplitude data arranged by phase window of
905 treatment showing paired recordings at that window for SCN with astrocytically expressed Gi-coupled
906 DREADDs treated with vehicle (grey, $N \geq 4$ at each phase) or 100nM CNO (pink, $N \geq 4$ at each phase).
907 Statistics: Šidák's multiple comparisons, $*p = 0.0401$. **G.** Summary cycle amplitude data arranged by
908 phase window of treatment showing paired recordings at that window for SCN with astrocytically
909 expressed Gi-coupled DREADDs treated with vehicle (grey, $N \geq 4$ at each phase) or 100nM CNO (pink,
910 $N \geq 4$ at each phase). **H.** Summary phase-shift data arranged by phase window of treatment showing
911 paired recordings at that phase window for SCN with astrocytically expressed Gi-coupled DREADDs
912 treated with vehicle (grey, $N \geq 4$ at each phase) or 100nM CNO (pink, $N \geq 4$ at each phase). In all

913 histogram plots, individual points joined by lines represent individual slices with paired treatment and
914 histogram bars with error bars represent mean \pm SEM.

915

916 **Figure 6: Chemogenetic activation of a Gq-coupled pathway in neurons, but not astrocytes,**
917 **resets SCN ensemble phase.**

918 **A.** Schematic showing cell-type-specific targeting of Gq-coupled DREADDs to neurons (*Syn-*
919 *hM3Dq::mCherry*), but not astrocytes in the intact SCN network (left) alongside representative PMT
920 traces showing acute vehicle (middle) and 100nM CNO (right) treatment during the CT0-6 time
921 window. The treatment interval is shown as a vertical line and coloured according to treatment:
922 vehicle (grey) or CNO (blue). **B.** Summary peak amplitude data arranged by phase window of
923 treatment showing paired recordings at that window for SCN with neuronally expressed Gq-coupled
924 DREADDs treated with vehicle (grey, $N \geq 7$ at each phase) or 100nM CNO (blue, $N \geq 7$ at each phase).
925 Statistics: Šidák's multiple comparisons, $**p = 0.006$, $****p < 0.0001$. **C.** Summary cycle amplitude data
926 arranged by phase window of treatment showing paired recordings at that window for SCN with
927 neuronally expressed Gq-coupled DREADDs treated with vehicle (grey, $N \geq 7$ at each phase) or 100nM
928 CNO (blue, $N \geq 7$ at each phase). Statistics: Šidák's multiple comparisons, $*p = 0.02$, $***p = 0.0006$. **D.**
929 Summary phase-shift data arranged by phase window of treatment showing paired recordings at that
930 phase window for SCN with neuronally expressed Gq-coupled DREADDs treated with vehicle (grey,
931 $N \geq 7$ at each phase) or 100nM CNO (blue, $N \geq 7$ at each phase). Statistics: Šidák's multiple
932 comparisons, $*p \leq 0.029$. **E.** Schematic showing cell-type-specific targeting of Gq-coupled DREADDs
933 to astrocytes (*GFAP-hM3Dq::mCherry*), but not neurons in the intact SCN network (left) alongside
934 representative PMT traces showing acute vehicle (middle) and 100nM CNO (right) treatment during
935 the CT0-6 time window. The treatment interval is shown as a vertical line and coloured according to
936 treatment: vehicle (grey) or CNO (pink). **F.** Summary peak amplitude data arranged by phase
937 window of treatment showing paired recordings at that window for SCN with astrocytically expressed
938 Gq-coupled DREADDs treated with vehicle (grey, $N \geq 5$ at each phase) or 100nM CNO (pink, $N \geq 5$ at
939 each phase). **G.** Summary cycle amplitude data arranged by phase window of treatment showing
940 paired recordings at that window for SCN with astrocytically expressed Gq-coupled DREADDs treated
941 with vehicle (grey, $N \geq 5$ at each phase) or 100nM CNO (pink, $N \geq 5$ at each phase). **H.** Summary

942 phase-shift data arranged by phase window of treatment showing paired recordings at that phase
943 window for SCN with astrocytically expressed Gq-coupled DREADDs treated with vehicle (grey, N≥5
944 at each phase) or 100nM CNO (pink, N≥5 at each phase). In all histogram plots, individual points
945 joined by lines represent individual slices with paired treatment and histogram bars with error bars
946 represent mean ±SEM.

947

948 **References**

- 949 Adamsky A, Kol A, Kreisel T, Doron A, Ozeri-Engelhard N, Melcer T, Refaeli R, Horn H, Regev L,
950 Groysman M, London M, Goshen I (2018) Astrocytic Activation Generates De Novo Neuronal
951 Potential and Memory Enhancement. Cell 174:59-71 e14.
- 952 Barca-Mayo O, Pons-Espinal M, Follert P, Armirotti A, Berdondini L, De Pietri Tonelli D (2017)
953 Astrocyte deletion of Bmal1 alters daily locomotor activity and cognitive functions via GABA
954 signalling. Nat Commun 8:14336.
- 955 Brancaccio M, Maywood ES, Chesham JE, Loudon AS, Hastings MH (2013) A Gq-Ca²⁺ axis controls
956 circuit-level encoding of circadian time in the suprachiasmatic nucleus. Neuron 78:714-728.
- 957 Brancaccio M, Patton AP, Chesham JE, Maywood ES, Hastings MH (2017) Astrocytes Control
958 Circadian Timekeeping in the Suprachiasmatic Nucleus via Glutamatergic Signaling. Neuron
959 93:1420-1435 e1425.
- 960 Brancaccio M, Edwards MD, Patton AP, Smyllie NJ, Chesham JE, Maywood ES, Hastings MH (2019)
961 Cell-autonomous clock of astrocytes drives circadian behavior in mammals. Science 363:187-
962 192.
- 963 Chai H, Diaz-Castro B, Shigetomi E, Monte E, Oceau JC, Yu X, Cohn W, Rajendran PS, Vondriska
964 TM, Whitelegge JP, Coppola G, Khakh BS (2017) Neural Circuit-Specialized Astrocytes:
965 Transcriptomic, Proteomic, Morphological, and Functional Evidence. Neuron 95:531-549
966 e539.
- 967 Colwell CS (2011) Linking neural activity and molecular oscillations in the SCN. Nat Rev Neurosci
968 12:553-569.
- 969 Dorostkar MM, Dreosti E, Odermatt B, Lagnado L (2010) Computational processing of optical
970 measurements of neuronal and synaptic activity in networks. J Neurosci Methods 188:141-
971 150.
- 972 Durkee CA, Covelo A, Lines J, Kofuji P, Aguilar J, Araque A (2019) Gi/o protein-coupled receptors
973 inhibit neurons but activate astrocytes and stimulate gliotransmission. Glia 67:1076-1093.
- 974 Edwards MD, Brancaccio M, Chesham JE, Maywood ES, Hastings MH (2016) Rhythmic expression
975 of cryptochrome induces the circadian clock of arrhythmic suprachiasmatic nuclei through
976 arginine vasopressin signaling. Proc Natl Acad Sci U S A 113:2732-2737.
- 977 Fonnum F, Johnsen A, Hassel B (1997) Use of fluorocitrate and fluoroacetate in the study of brain
978 metabolism. Glia 21:106-113.
- 979 Gribkoff VK, Pieschl RL, Wisialowski TA, van den Pol AN, Yocca FD (1998) Phase shifting of
980 circadian rhythms and depression of neuronal activity in the rat suprachiasmatic nucleus by
981 neuropeptide Y: mediation by different receptor subtypes. J Neurosci 18:3014-3022.
- 982 Guldner FH (1983) Numbers of neurons and astroglial cells in the suprachiasmatic nucleus of male
983 and female rats. Exp Brain Res 50:373-376.
- 984 Hablitz LM, Gunesch AN, Cravetchi O, Moldavan M, Allen CN (2020) Cannabinoid Signaling Recruits
985 Astrocytes to Modulate Presynaptic Function in the Suprachiasmatic Nucleus. eNeuro 7.
- 986 Halassa MM, Fellin T, Takano H, Dong JH, Haydon PG (2007) Synaptic islands defined by the
987 territory of a single astrocyte. J Neurosci 27:6473-6477.
- 988 Hamnett R, Crosby P, Chesham JE, Hastings MH (2019) Vasoactive intestinal peptide controls the
989 suprachiasmatic circadian clock network via ERK1/2 and DUSP4 signalling. Nat Commun
990 10:542.
- 991 Hamnett R, Chesham JE, Maywood ES, Hastings MH (2021) The Cell-Autonomous Clock of VIP
992 Receptor VPAC2 Cells Regulates Period and Coherence of Circadian Behavior. J Neurosci
993 41:502-512.
- 994 Hassel B, Westergaard N, Schousboe A, Fonnum F (1995) Metabolic differences between primary
995 cultures of astrocytes and neurons from cerebellum and cerebral cortex. Effects of
996 fluorocitrate. Neurochem Res 20:413-420.
- 997 Hastings MH, Maywood ES, Brancaccio M (2018) Generation of circadian rhythms in the
998 suprachiasmatic nucleus. Nat Rev Neurosci 19:453-469.
- 999 Hastings MH, Reddy AB, McMahon DG, Maywood ES (2005) Analysis of circadian mechanisms in the
1000 suprachiasmatic nucleus by transgenesis and biolistic transfection. Methods Enzymol
1001 393:579-592.
- 1002 Haustein MD, Kracun S, Lu XH, Shih T, Jackson-Weaver O, Tong X, Xu J, Yang XW, O'Dell TJ,
1003 Marvin JS, Ellisman MH, Bushong EA, Looger LL, Khakh BS (2014) Conditions and
1004 constraints for astrocyte calcium signaling in the hippocampal mossy fiber pathway. Neuron
1005 82:413-429.

- 1006 Jones JR, Tackenberg MC, McMahon DG (2015) Manipulating circadian clock neuron firing rate
1007 resets molecular circadian rhythms and behavior. *Nat Neurosci* 18:373-375.
- 1008 Lee IT, Chang AS, Manandhar M, Shan Y, Fan J, Izumo M, Ikeda Y, Motoike T, Dixon S, Seinfeld JE,
1009 Takahashi JS, Yanagisawa M (2015) Neuromedin s-producing neurons act as essential
1010 pacemakers in the suprachiasmatic nucleus to couple clock neurons and dictate circadian
1011 rhythms. *Neuron* 85:1086-1102.
- 1012 Manvich DF, Webster KA, Foster SL, Farrell MS, Ritchie JC, Porter JH, Weinschenker D (2018) The
1013 DREADD agonist clozapine N-oxide (CNO) is reverse-metabolized to clozapine and produces
1014 clozapine-like interoceptive stimulus effects in rats and mice. *Sci Rep* 8:3840.
- 1015 Marpegan L, Krall TJ, Herzog ED (2009) Vasoactive intestinal polypeptide entrains circadian rhythms
1016 in astrocytes. *J Biol Rhythms* 24:135-143.
- 1017 Martin-Fernandez M, Jamison S, Robin LM, Zhao Z, Martin ED, Aguilar J, Benneyworth MA,
1018 Marsicano G, Araque A (2017) Synapse-specific astrocyte gating of amygdala-related
1019 behavior. *Nat Neurosci* 20:1540-1548.
- 1020 Maywood ES, Mrosovsky N, Field MD, Hastings MH (1999) Rapid down-regulation of mammalian
1021 period genes during behavioral resetting of the circadian clock. *Proc Natl Acad Sci U S A*
1022 96:15211-15216.
- 1023 Maywood ES, Reddy AB, Wong GK, O'Neill JS, O'Brien JA, McMahon DG, Harmor AJ, Okamura H,
1024 Hastings MH (2006) Synchronization and maintenance of timekeeping in suprachiasmatic
1025 circadian clock cells by neuropeptidergic signaling. *Curr Biol* 16:599-605.
- 1026 Maywood ES, Elliott TS, Patton AP, Krogager TP, Chesham JE, Ernst RJ, Beranek V, Brancaccio M,
1027 Chin JW, Hastings MH (2018) Translational switching of Cry1 protein expression confers
1028 reversible control of circadian behavior in arrhythmic Cry-deficient mice. *Proc Natl Acad Sci U*
1029 *S A* 115:E12388-E12397.
- 1030 Meijer JH, Schwartz WJ (2003) In search of the pathways for light-induced pacemaker resetting in the
1031 suprachiasmatic nucleus. *J Biol Rhythms* 18:235-249.
- 1032 Mieda M, Ono D, Hasegawa E, Okamoto H, Honma K, Honma S, Sakurai T (2015) Cellular clocks in
1033 AVP neurons of the SCN are critical for interneuronal coupling regulating circadian behavior
1034 rhythm. *Neuron* 85:1103-1116.
- 1035 Moore A, Zielinski T, Millar AJ (2014) Online period estimation and determination of rhythmicity in
1036 circadian data, using the BioDare data infrastructure. *Methods Mol Biol* 1158:13-44.
- 1037 Moore RY, Bernstein ME (1989) Synaptogenesis in the rat suprachiasmatic nucleus demonstrated by
1038 electron microscopy and synapsin I immunoreactivity. *J Neurosci* 9:2151-2162.
- 1039 Morin LP, Allen CN (2006) The circadian visual system, 2005. *Brain Res Rev* 51:1-60.
- 1040 Morris EL, Patton AP, Chesham JE, Crisp A, Adamson A, Hastings MH (2021) Single-cell
1041 transcriptomics of suprachiasmatic nuclei reveal a Prokineticin-driven circadian network.
1042 *EMBO J* 40:e108614.
- 1043 Nagai J, Rajbhandari AK, Gangwani MR, Hachisuka A, Coppola G, Masmanidis SC, Fanselow MS,
1044 Khakh BS (2019) Hyperactivity with Disrupted Attention by Activation of an Astrocyte
1045 Synaptogenic Cue. *Cell* 177:1280-1292 e1220.
- 1046 Ono D, Honma KI, Schmal C, Takumi T, Kawamoto T, Fujimoto K, Kato Y, Honma S (2021)
1047 CHRONO and DEC1/DEC2 compensate for lack of CRY1/CRY2 in expression of coherent
1048 circadian rhythm but not in generation of circadian oscillation in the neonatal mouse SCN. *Sci*
1049 *Rep* 11:19240.
- 1050 Partch CL, Green CB, Takahashi JS (2014) Molecular architecture of the mammalian circadian clock.
1051 *Trends in cell biology* 24:90-99.
- 1052 Patton AP, Hastings MH (2018) The suprachiasmatic nucleus. *Curr Biol* 28:R816-R822.
- 1053 Patton AP, Chesham JE, Hastings MH (2016) Combined Pharmacological and Genetic Manipulations
1054 Unlock Unprecedented Temporal Elasticity and Reveal Phase-Specific Modulation of the
1055 Molecular Circadian Clock of the Mouse Suprachiasmatic Nucleus. *J Neurosci* 36:9326-9341.
- 1056 Patton AP, Edwards MD, Smyllie NJ, Hamnett R, Chesham JE, Brancaccio M, Maywood ES,
1057 Hastings MH (2020) The VIP-VPAC2 neuropeptidergic axis is a cellular pacemaking hub of
1058 the suprachiasmatic nucleus circadian circuit. *Nature communications* 11:3394.
- 1059 Paulsen RE, Contestabile A, Villani L, Fonnum F (1987) An in vivo model for studying function of
1060 brain tissue temporarily devoid of glial cell metabolism: the use of fluorocitrate. *J Neurochem*
1061 48:1377-1385.
- 1062 Perea G, Navarrete M, Araque A (2009) Tripartite synapses: astrocytes process and control synaptic
1063 information. *Trends Neurosci* 32:421-431.
- 1064 Price TS, Baggs JE, Curtis AM, Fitzgerald GA, Hogenesch JB (2008) WAVECLOCK: wavelet analysis
1065 of circadian oscillation. *Bioinformatics* 24:2794-2795.

- 1066 Prolo LM, Takahashi JS, Herzog ED (2005) Circadian rhythm generation and entrainment in
1067 astrocytes. *J Neurosci* 25:404-408.
- 1068 Prosser RA, Edgar DM, Heller HC, Miller JD (1994) A possible glial role in the mammalian circadian
1069 clock. *Brain Res* 643:296-301.
- 1070 Reppert SM, Weaver DR (2002) Coordination of circadian timing in mammals. *Nature* 418:935-941.
- 1071 Roth BL (2016) DREADDs for Neuroscientists. *Neuron* 89:683-694.
- 1072 Schindelin J, Arganda-Carreras I, Frise E, Kaynig V, Longair M, Pietzsch T, Preibisch S, Rueden C,
1073 Saalfeld S, Schmid B, Tinevez JY, White DJ, Hartenstein V, Eliceiri K, Tomancak P, Cardona
1074 A (2012) Fiji: an open-source platform for biological-image analysis. *Nat Methods* 9:676-682.
- 1075 Semyanov A, Henneberger C, Agarwal A (2020) Making sense of astrocytic calcium signals - from
1076 acquisition to interpretation. *Nat Rev Neurosci* 21:551-564.
- 1077 Shan Y, Abel JH, Li Y, Izumo M, Cox KH, Jeong B, Yoo SH, Olson DP, Doyle FJ, 3rd, Takahashi JS
1078 (2020) Dual-Color Single-Cell Imaging of the Suprachiasmatic Nucleus Reveals a Circadian
1079 Role in Network Synchrony. *Neuron* 108:164-179 e167.
- 1080 Shearman LP, Zylka MJ, Weaver DR, Kolakowski LF, Jr., Reppert SM (1997) Two period homologs:
1081 circadian expression and photic regulation in the suprachiasmatic nuclei. *Neuron* 19:1261-
1082 1269.
- 1083 Shen W, Chen S, Liu Y, Han P, Ma T, Zeng LH (2021) Chemogenetic manipulation of astrocytic
1084 activity: Is it possible to reveal the roles of astrocytes? *Biochem Pharmacol* 186:114457.
- 1085 Smyllie NJ, Chesham JE, Hamnett R, Maywood ES, Hastings MH (2016) Temporally chimeric mice
1086 reveal flexibility of circadian period-setting in the suprachiasmatic nucleus. *Proc Natl Acad Sci*
1087 *U S A* 113:3657-3662.
- 1088 Smyllie NJ, Bagnall J, Koch AA, Niranjan D, Polidarova L, Chesham JE, Chin JW, Partch CL, Loudon
1089 AS, Hastings MH (2022) Cryptochrome proteins regulate the circadian intracellular behavior
1090 and localization of PER2 in mouse suprachiasmatic nucleus neurons. *Proc Natl Acad Sci U S*
1091 *A* 119.
- 1092 Sueviriyapan N, Tso CF, Herzog ED, Henson MA (2020) Astrocytic Modulation of Neuronal Activity in
1093 the Suprachiasmatic Nucleus: Insights from Mathematical Modeling. *J Biol Rhythms* 35:287-
1094 301.
- 1095 Swanson RA, Graham SH (1994) Fluorocitrate and fluoroacetate effects on astrocyte metabolism in
1096 vitro. *Brain Res* 664:94-100.
- 1097 Travnickova-Bendova Z, Cermakian N, Reppert SM, Sassone-Corsi P (2002) Bimodal regulation of
1098 mPeriod promoters by CREB-dependent signaling and CLOCK/BMAL1 activity. *Proc Natl*
1099 *Acad Sci U S A* 99:7728-7733.
- 1100 Tso CF, Simon T, Greenlaw AC, Puri T, Mieda M, Herzog ED (2017) Astrocytes Regulate Daily
1101 Rhythms in the Suprachiasmatic Nucleus and Behavior. *Curr Biol* 27:1055-1061.
- 1102 Vaidyanathan TV, Collard M, Yokoyama S, Reitman ME, Poskanzer KE (2021) Cortical astrocytes
1103 independently regulate sleep depth and duration via separate GPCR pathways. *Elife* 10.
- 1104 van der Horst GT, Muijtjens M, Kobayashi K, Takano R, Kanno S, Takao M, de Wit J, Verkerk A, Eker
1105 AP, van Leenen D, Buijs R, Bootsma D, Hoeijmakers JH, Yasui A (1999) Mammalian Cry1
1106 and Cry2 are essential for maintenance of circadian rhythms. *Nature* 398:627-630.
- 1107 van der Vinne V, Swoap SJ, Vaitay TJ, Weaver DR (2018) Desynchrony between brain and
1108 peripheral clocks caused by CK1delta/epsilon disruption in GABA neurons does not lead to
1109 adverse metabolic outcomes. *Proc Natl Acad Sci U S A* 115:E2437-E2446.
- 1110 Yamaguchi S, Isejima H, Matsuo T, Okura R, Yagita K, Kobayashi M, Okamura H (2003)
1111 Synchronization of cellular clocks in the suprachiasmatic nucleus. *Science* 302:1408-1412.
- 1112 Yoo SH, Yamazaki S, Lowrey PL, Shimomura K, Ko CH, Buhr ED, Slepka SM, Hong HK, Oh WJ, Yoo
1113 OJ, Menaker M, Takahashi JS (2004) PERIOD2::LUCIFERASE real-time reporting of
1114 circadian dynamics reveals persistent circadian oscillations in mouse peripheral tissues. *Proc*
1115 *Natl Acad Sci U S A* 101:5339-5346.
- 1116 Yu X, Nagai J, Khakh BS (2020) Improved tools to study astrocytes. *Nat Rev Neurosci* 21:121-138.
- 1117 Zielinski T, Moore AM, Troup E, Halliday KJ, Millar AJ (2014) Strengths and limitations of period
1118 estimation methods for circadian data. *PLoS One* 9:e96462.
- 1119

Figure 1

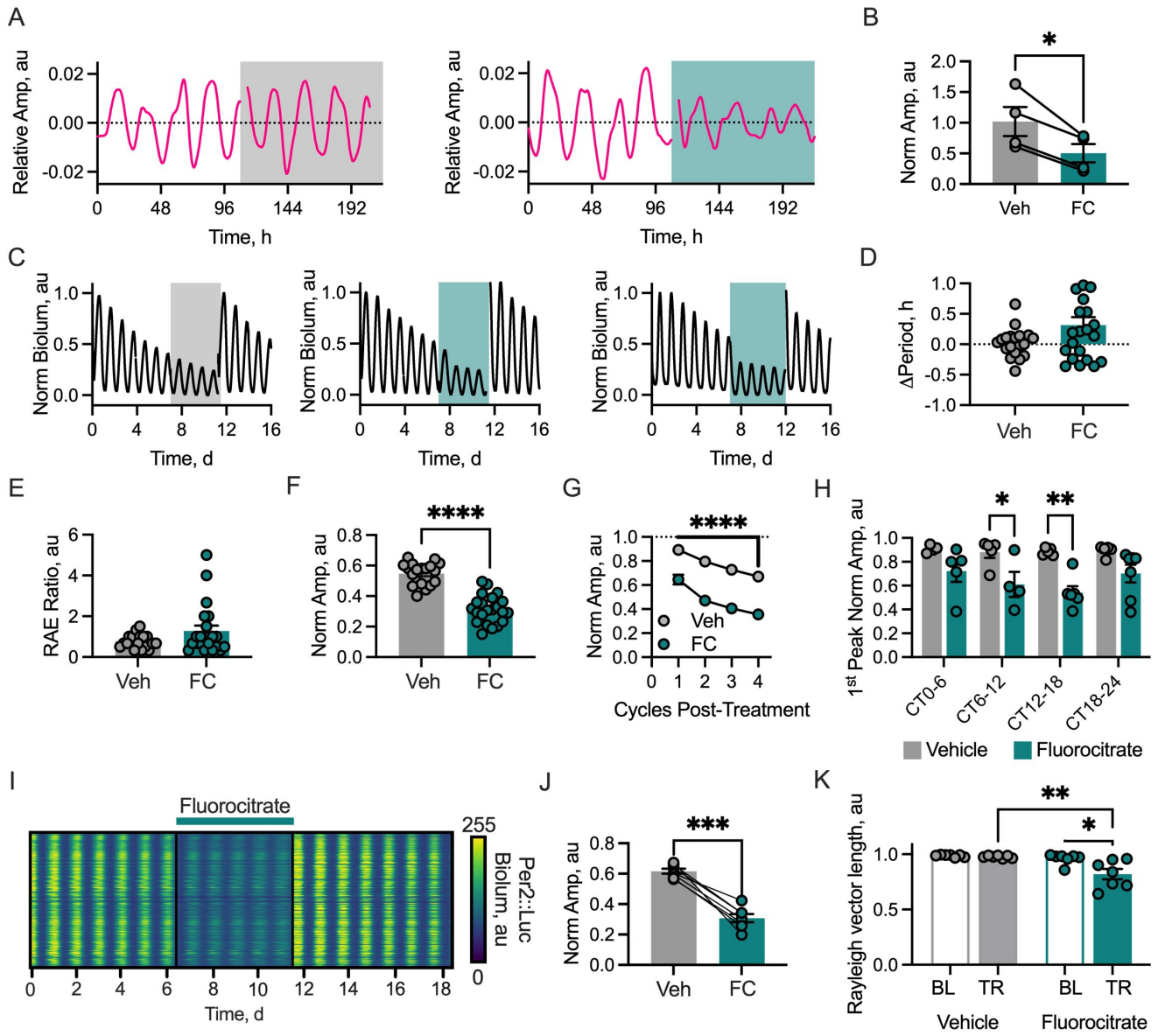


Figure 2

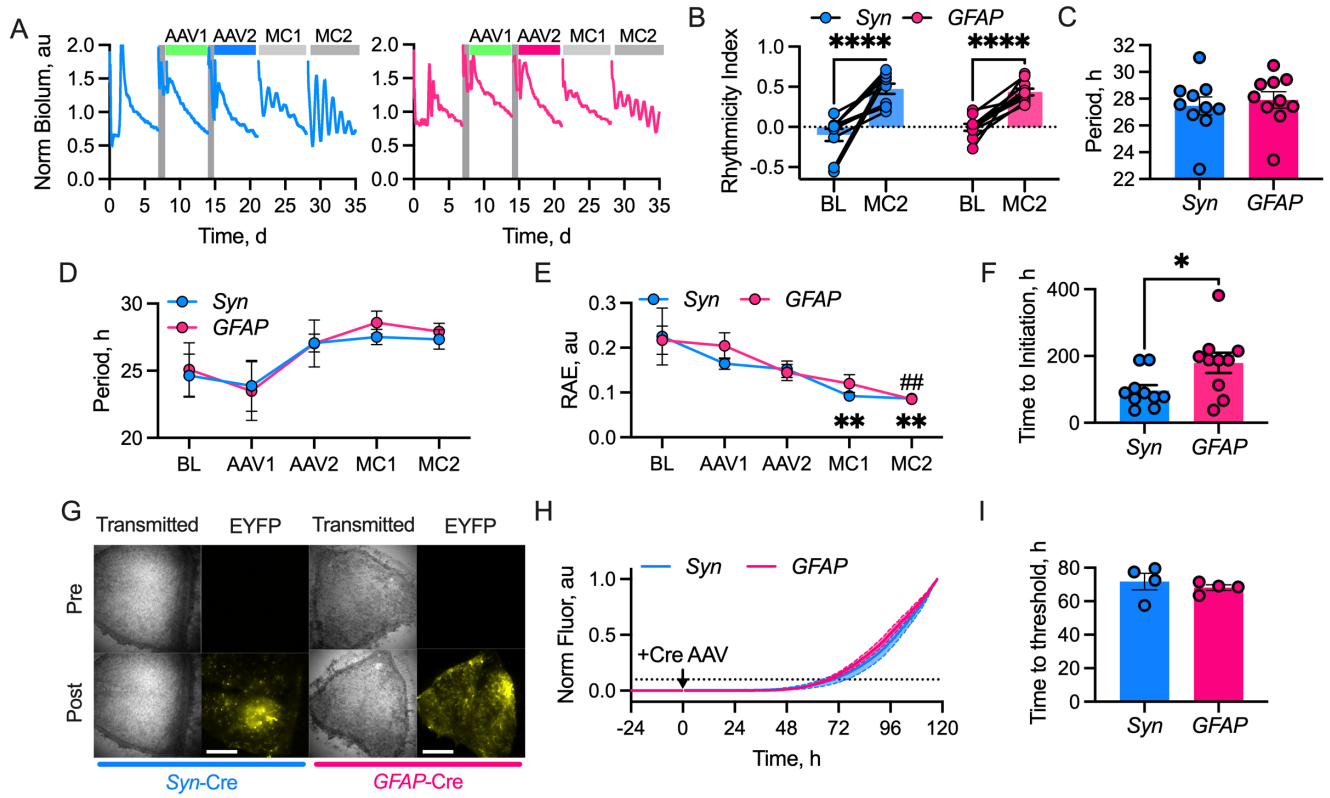


Figure 3

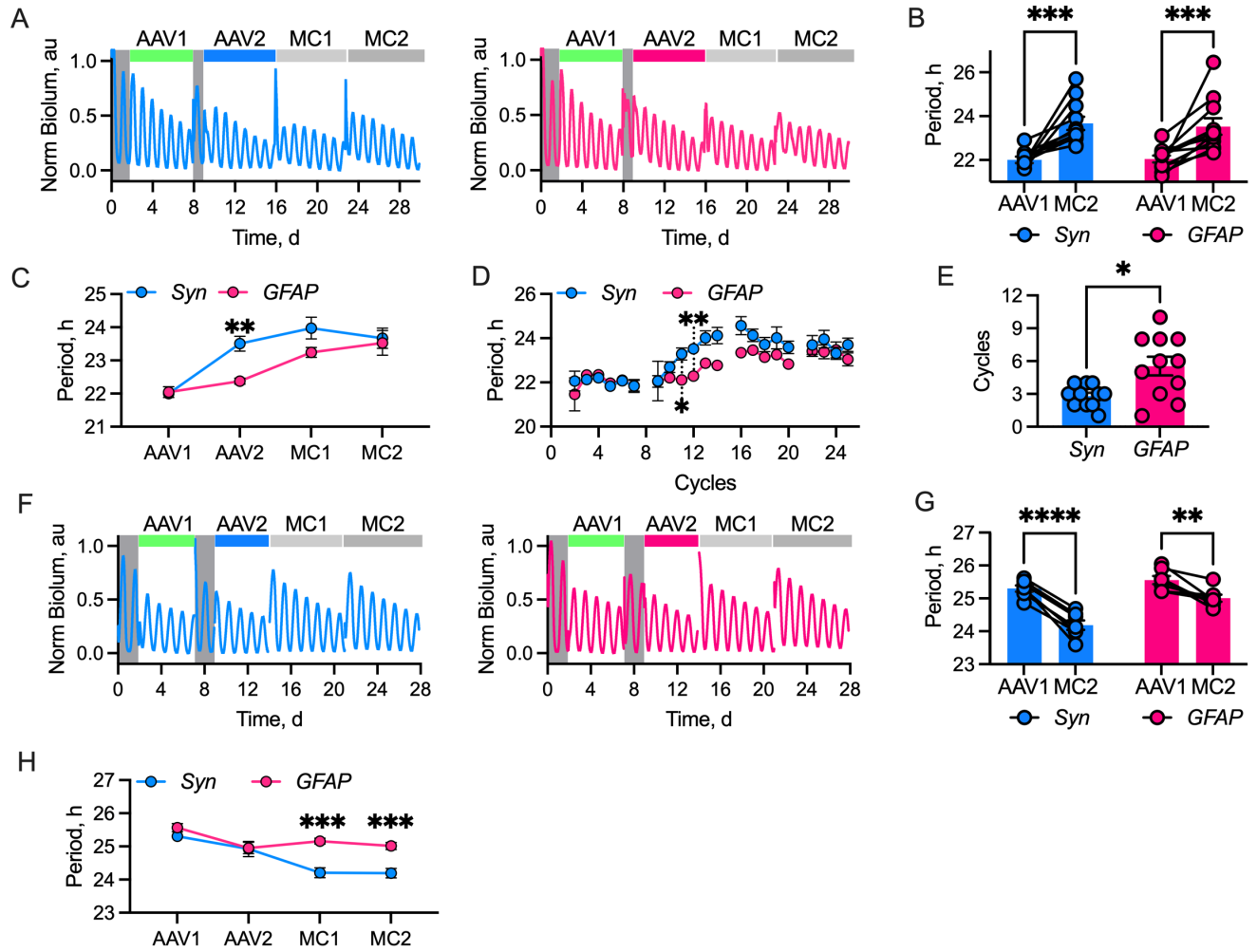


Figure 4

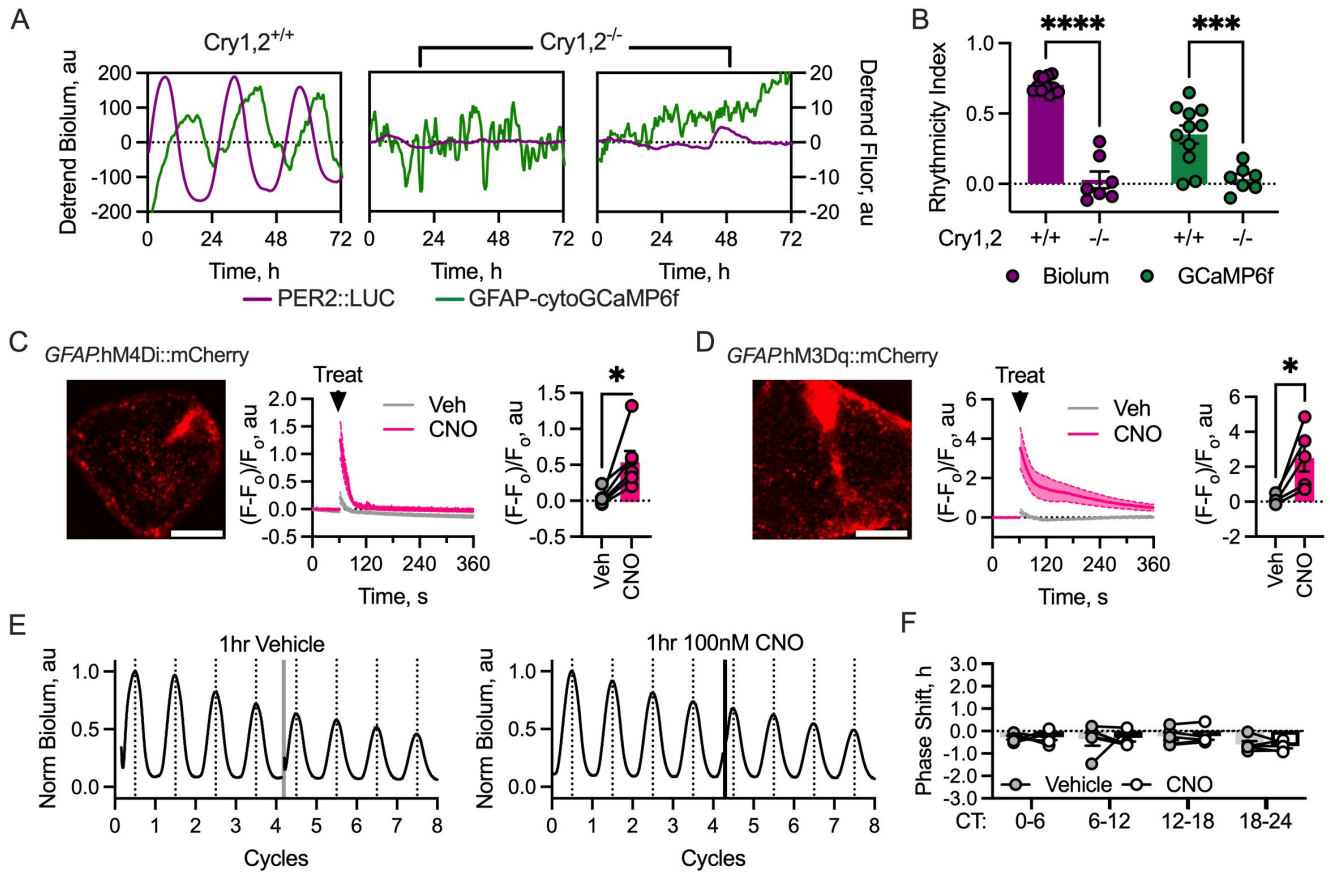


Figure 5

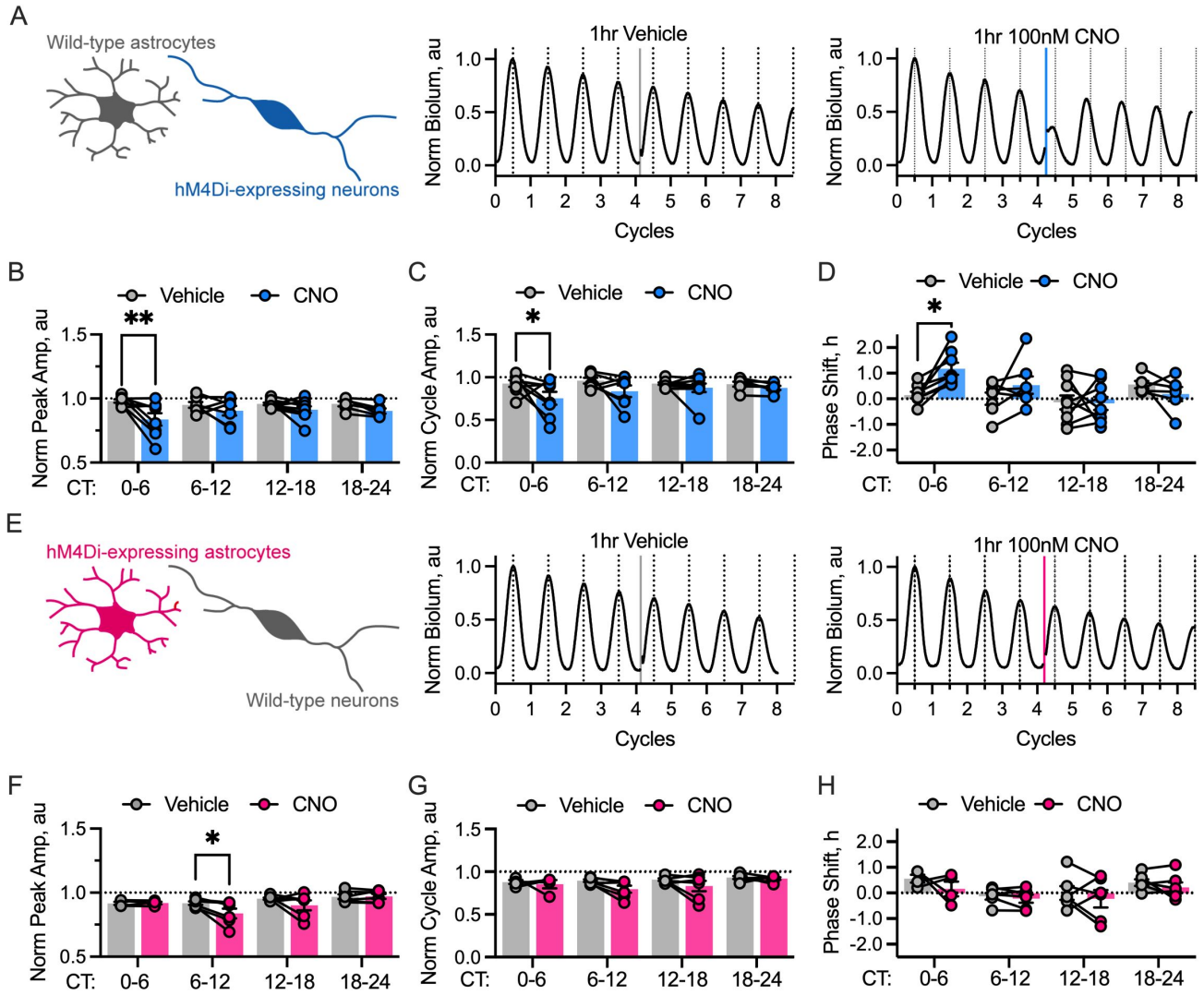


Figure 6

